



# High-entropy spinel oxide ( $\text{Fe}_{0.2}\text{Mg}_{0.2}\text{Mn}_{0.1}\text{Al}_{0.3}\text{Cr}_{0.2}$ )<sub>3</sub>O<sub>4</sub> as a highly active and stable redox material for methane driven solar thermochemical water splitting

Yujia Han <sup>a,b</sup>, Ming Tian <sup>a,\*</sup>, Chaojie Wang <sup>a,b</sup>, Teng Zong <sup>a,b</sup>, Xiaodong Wang <sup>a,\*</sup>

<sup>a</sup> CAS Key Laboratory of Science and Technology on Applied Catalysis, Dalian Institute of Chemical Physics, Chinese Academy of Sciences, 457 Zhongshan Road, Dalian 116023, People's Republic of China

<sup>b</sup> University of Chinese Academy of Sciences, 19(A) Yuquan Road, Shijingshan District, Beijing 100049, People's Republic of China



## ARTICLE INFO

### Keywords:

High-entropy spinel oxide  
Methane driven solar water splitting  
Self-regeneration of metal  
 $\text{H}_2\text{O}$  activation  
Cycling stability

## ABSTRACT

Solar thermochemical  $\text{H}_2\text{O}$  splitting has attained wide attention as a promising solution for hydrogen production. However, it remains a daunting challenge to produce hydrogen with high kinetics and stability for the oxide materials at lower temperature because of insufficient active sites for  $\text{H}_2\text{O}$  activation and splitting. Herein, we report a high-entropy spinel oxide that consists of five cations (HEO) and can highly-effectively thermochemically split  $\text{H}_2\text{O}$  to  $\text{H}_2$  with ultrahigh production rate and productivity of  $182.9 \text{ mL min}^{-1} \text{ g}^{-1}$  and  $68.5 \text{ mL g}^{-1}$ , respectively, several times higher than state-of-the-art materials via a two-step cycle process with methane driven reduction. High-entropy effect facilitated the preservation of single-phase structure even at large amount of oxygen converted (almost  $70 \text{ mL g}^{-1}$ ), which promoted the exsolution and stabilization of substantial  $\text{Fe}^0$  nanoparticles (20–30 nm vs. 100 nm) and their dissolution into spinel structure during redox process, resulting in extensive metal-oxide interfaces with metal-oxygen vacancy pairs responsible for the efficient and stable water splitting. Such findings provide a class of viable material with high configurational entropy for efficient hydrogen generation.

## 1. Introduction

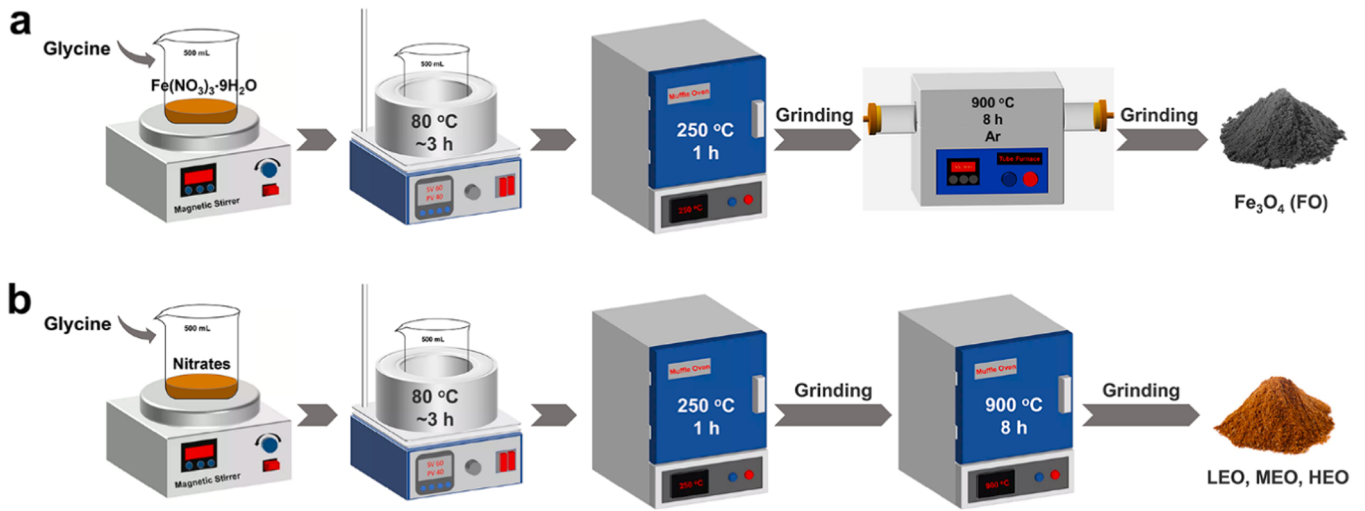
The conversion of solar energy is one of the most attractive approaches to alleviate energy and environmental problems [1–3]. However, due to the intermittent and uneven distribution of solar radiation, energy from the sun must be efficiently converted into high value-added chemical fuels for storage, transportation and usage [4–6]. Hydrogen with high energy density and pollution-free characteristics is an efficient and clean energy carrier and a valuable chemical precursor for renewable energy industrial systems [7]. Two-step solar thermochemical water splitting (STWS) has received considerable attention as an attractive technology for hydrogen production compared with other three artificial catalytic processes (electrocatalysis, photocatalysis, and photoelectrocatalysis) [8,9] due to the utilization of the entire solar spectrum, simplification of gas separation and higher hydrogen evolution rate [10]. In the two-step redox cycle, the reducible metal oxides are first reduced at high temperature (above  $1400^\circ\text{C}$ ) and low oxygen partial pressures using concentrated solar radiation and then the metal

oxides with oxygen deficiencies are re-oxidized by water vapor under lower temperature to release hydrogen. However, the large temperature swing between the two steps decreases the thermodynamic efficiency and poses serious challenges on the design of reactor and structure of materials [11]. In the last 10 years, thermochemical cycles have moved towards to lower temperatures of  $\sim 1100^\circ\text{C}$  [12,13]. Alternatively, introducing reducing agents such as methane can significantly reduce the reduction temperature ( $\leq 900^\circ\text{C}$ ) and oxygen partial pressure to achieve isothermal thermochemical water splitting (methane driven reduction, MDR-STWS), thereby enhancing lattice oxygen extraction from metal oxides and the productivity of hydrogen [9,14–16].

The key challenges of the two-step MDR-STWS are to achieve high hydrogen production rate and productivity as well as long-term stability, which have stringent requirements for metal oxides as the redox intermediates. The state-of-the-art (substituted) cerium oxide materials [9,10,14,17–19] have been extensively investigated thanks to their high  $\text{H}_2$  production rate due to the abundant oxygen vacancies that facilitate the activation of  $\text{H}_2\text{O}$ . However, it usually suffers from inferior  $\text{H}_2$

\* Corresponding authors.

E-mail addresses: [tm1982@dicp.ac.cn](mailto:tm1982@dicp.ac.cn) (M. Tian), [xdwang@dicp.ac.cn](mailto:xdwang@dicp.ac.cn) (X. Wang).



**Scheme 1.** Schematic illustrations of the synthesis of (a) FO, (b) LEO, MEO, and HEO via a combustion method.

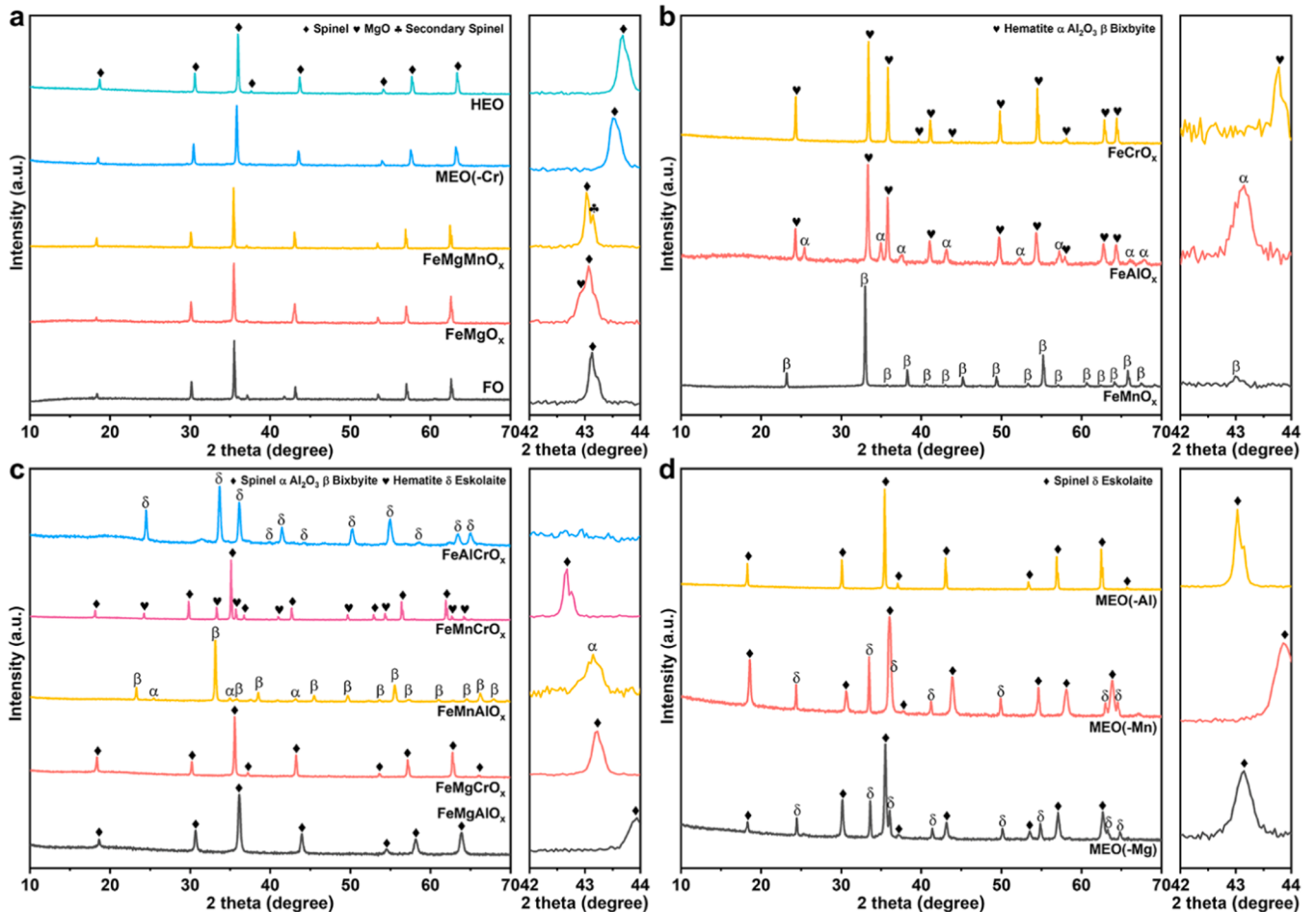


**Fig. 1.** XRD patterns of as synthesized (a) FO, FeMgO<sub>x</sub>, FeMgMnO<sub>x</sub>, MEO(-Cr), HEO, other (b) binary, (c) ternary, and (d) quaternary oxides, and their corresponding magnified views in the range of 42–44 degree (2 theta). The unobvious shoulder peaks around 43.8 degree (2 theta) in the magnified views of some samples (such as in HEO, MEO(-Cr) and FO in Fig. 1a) could be resulted from the scanning errors of instrument originating from  $K_{\alpha 1}$  and  $K_{\alpha 2}$  rays of the Cu target (usually  $K_{\alpha 2}/K_{\alpha 1} = 0.5$ ) [63,64]. The more obvious peak splitting marked in the magnified views can be attributed to different phases (such as in FeMgMnO<sub>x</sub> in Fig. 1a), which can also be confirmed by EDS mapping (Fig. S2).

productivity induced by insufficient activation of  $\text{CH}_4$  and thus low oxygen exchange capacity. Recent studies indicated that the productivity of hydrogen of (substituted) cerium oxides can be significantly

enhanced by introducing certain amounts of active metal species to improve  $\text{CH}_4$  and lattice oxygen activation such as the transition metal Ni [9,14] and platinum group noble metal [20–22]. Unfortunately,

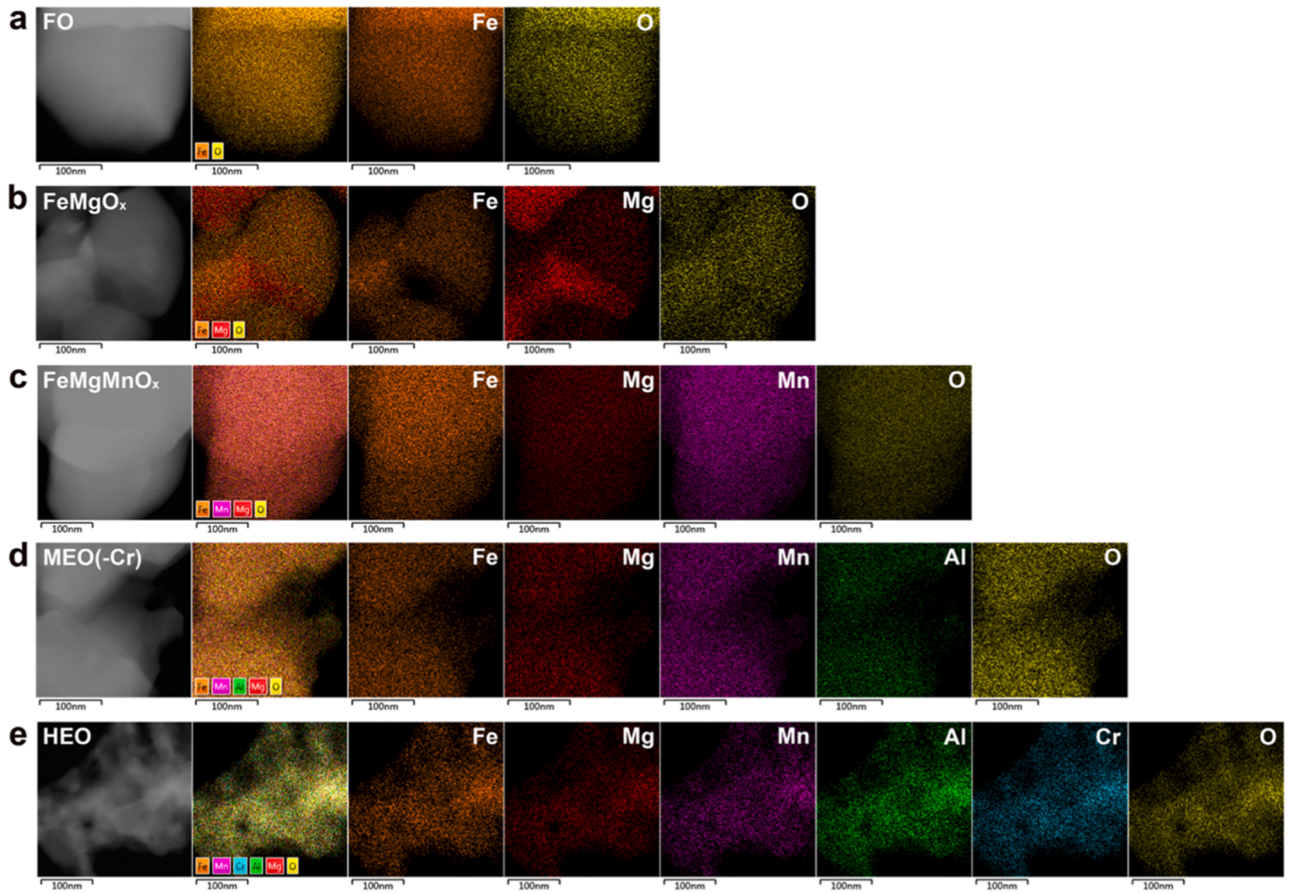


Fig. 2. EDS element mappings of as synthesized redox materials. (a) FO, (b) FeMgO<sub>x</sub>, (c) FeMgMnO<sub>x</sub>, (d) MEO(-Cr), and (e) HEO.

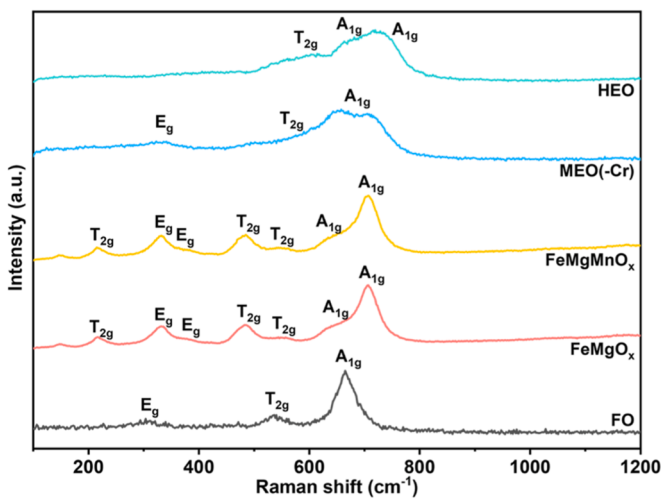


Fig. 3. Raman spectra of as synthesized FO, FeMgO<sub>x</sub>, FeMgMnO<sub>x</sub>, MEO(-Cr) and HEO. As the number of the metal species increases, the peak of A<sub>1g</sub> shows a broad shape, indicating that HEO has a high degree of disorder [51,52].

active metals sinter severely during multiple redox cycles under high temperature, which brings about limited exposed surface or metal-support interface with oxygen vacancies and thus decreased H<sub>2</sub>O activation. To address the challenge, researchers doped active metals into oxides such as perovskites [23–26] and spinels [27] to improve their sinter-resistance by in-situ exsolution and dissolution during redox cycles. The amount of oxygen converted has to be delicately controlled

since excessive reduction will lead to the collapse of host matrix causing the agglomeration of nanoparticles and phase segregation thus the deactivation of performance during redox cycles [25,27]. This also induces insufficient active sites (metal or oxygen vacancy) in the surface or interface for H<sub>2</sub>O activation so that hydrogen production rate remains unsatisfactory [28,29].

High-entropy oxide (HEO) first reported in 2015 is a kind of multicationic solid solution materials with five or more elements in near-equiatomic proportion containing various styles such as spinel, perovskite, rock-salt and fluorite crystal structures [30]. It is considered that the configurational entropy of HEOs is larger than 1.5 R ( $\Delta S_{conf} > 1.5$  R) according to the ideal configurational entropy concept ( $\Delta S_{conf} = -R \sum_{i=1}^n x_i \ln x_i$ , where R is the gas constant and  $x_i$  is the mole fraction of the i<sup>th</sup> component). Based on the Gibbs–Helmholtz equation ( $\Delta G_{mix} = \Delta H_{mix} - T\Delta S_{mix}$ ), higher configurational entropy promotes the stability of the compound because of the more negative  $\Delta G_{mix}$  especially under high temperature. Furthermore, recent research work indeed reported ultrahigh stability of HEO in the application of heterogeneous catalysis [31–33]. As a result, we envision that the entropy stabilization and entropy-added motivation could be favorable for the preservation of host structure even at extensive reduction during the exsolution of metal nanoparticles and back into parent metal oxides, which would inhibit the sintering of active metal nanoparticles so that abundant metal sites and oxygen vacancies can improve H<sub>2</sub>O activation to achieve high H<sub>2</sub> production rate and productivity in solar thermochemical H<sub>2</sub>O splitting. To the best of our knowledge, HEO materials have been few studied in the STWS [34–37].

In the current work, we verified the entropy-driven principle in two-step STWS process by a high-entropy oxide with spinel structure (Fe<sub>3</sub>O<sub>4</sub>) which usually suffers from deactivation induced by severe sintering of

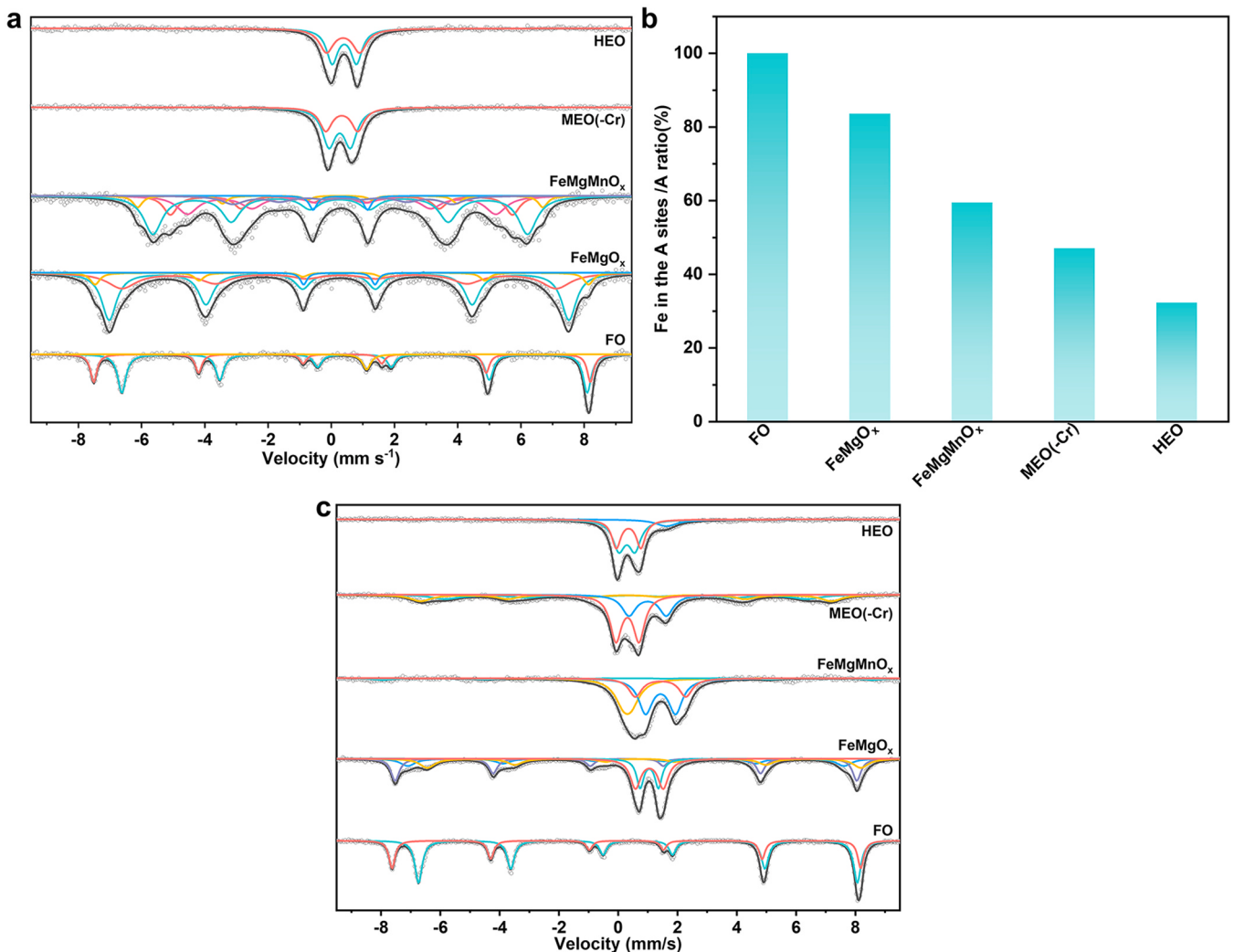


**Fig. 4.** (a) <sup>57</sup>Fe Mössbauer spectra and (b) the corresponding quantitative results of Fe in the A sites/A of as synthesized FO, FeMgO<sub>x</sub>, FeMgMnO<sub>x</sub>, MEO(-Cr) and HEO. (c) <sup>57</sup>Fe Mössbauer spectra of FO, FeMgO<sub>x</sub>, FeMgMnO<sub>x</sub>, MEO(-Cr) and HEO after 10 cycles.

active sites and destruction of structure during multiple redox cycles. Specifically, a single-phase cubic ( $\text{Fe}_{0.2}\text{Mg}_{0.2}\text{Mn}_{0.1}\text{Al}_{0.3}\text{Cr}_{0.2}$ )<sub>3</sub>O<sub>4</sub> was prepared and selected considering that Mg and Al could enhance the anti-sintering while Cr and Mn were more difficult to be reduced to metallic state and thus only  $\text{Fe}^0$  nanoparticles or  $\text{Fe}^0/\text{HEO}$  interfaces were regarded to be active sites for  $\text{H}_2\text{O}$  activation. Encouragingly, it achieved remarkable improvement of performance for two-step MDR-STWS with peak  $\text{H}_2$  evolution rate of  $182.9 \text{ mL min}^{-1} \text{ g}^{-1}$  and total  $\text{H}_2$  productivity of  $68.5 \text{ mL g}^{-1}$  without obvious degradation of reactivity during 10 redox cycles, which far exceeded  $\text{Fe}_3\text{O}_4$ , other binary, ternary (low entropy, LEO) and quaternary (medium entropy, MEO) metal oxides as well as the state-of-the-art  $\text{CeO}_2$  and perovskite oxides. Such the superior performance was attributed to the entropy-stabilized spinel structure even at large amount of oxygen converted (almost  $70 \text{ mL g}^{-1}$ ), promoting the exsolution and stabilization of massive  $\text{Fe}^0$  nanoparticles, which brought about abundant  $\text{Fe}^0/\text{HEO}$  interfaces with more metal-oxygen vacancy pairs for  $\text{H}_2\text{O}$  activation and splitting. Moreover, the reintegration of metal nanoparticles into HEO occurred more easily than other LEO and MEO due to the entropy motivation, improving the efficiency and stability of MDR-STWS. The excellent talent of high-entropy oxides for redox reactions may provide an alternative for the design of artificial redox materials for efficient hydrogen generation.

## 2. Experiment

### 2.1. Redox materials synthesis

The iron-based spinel redox materials were prepared via a wet chemical process [38], using  $\text{Fe}(\text{NO}_3)_3 \cdot 9 \text{ H}_2\text{O}$  (Aladdin, China),  $\text{Mg}(\text{NO}_3)_2 \cdot 6 \text{ H}_2\text{O}$  (Damao, China), 50 wt%  $\text{Mn}(\text{NO}_3)_2$  solution (Damao, China),  $\text{Al}(\text{NO}_3)_3 \cdot 9 \text{ H}_2\text{O}$  (Aladdin, China), and  $\text{Cr}(\text{NO}_3)_3 \cdot 9 \text{ H}_2\text{O}$  (Aladdin, China) as precursors and glycine (Aladdin, China) as an additive. Typically, 4.8 mmol  $\text{Fe}(\text{NO}_3)_3 \cdot 9 \text{ H}_2\text{O}$ , 4.8 mmol  $\text{Mg}(\text{NO}_3)_2 \cdot 6 \text{ H}_2\text{O}$ , 2.4 mmol 50 wt%  $\text{Mn}(\text{NO}_3)_2$  solution, 7.2 mmol  $\text{Al}(\text{NO}_3)_3 \cdot 9 \text{ H}_2\text{O}$ , and 4.8 mmol  $\text{Cr}(\text{NO}_3)_3 \cdot 9 \text{ H}_2\text{O}$  were dissolved in ultrapure water (48 mL) with magnetic stirring. After that, 4.504 g glycine was added under continuously stirring, and then the obtained homogenous dark brown solution was heated at  $80^\circ\text{C}$  for about 3 h to vaporize the solvent and further heated at  $250^\circ\text{C}$  under stagnant air for 1 h to gain dried intermediate. The dried intermediate was ground into a fine powder, which was then transferred to a muffle oven and calcined at  $900^\circ\text{C}$  for 8 h (at a heating rate of  $5^\circ\text{C min}^{-1}$ ) to produce  $(\text{Fe}_{0.2}\text{Mg}_{0.2}\text{Mn}_{0.1}\text{Al}_{0.3}\text{Cr}_{0.2})_3\text{O}_4$  (designated as HEO). For comparison, the following oxides were prepared using the same method:  $\text{Fe}_3\text{O}_4$  (FO, calcined at  $900^\circ\text{C}$  for 8 h under Ar atmosphere),  $\text{FeMgO}_x$ ,  $\text{FeMnO}_x$ ,  $\text{FeAlO}_x$ ,  $\text{FeCrO}_x$ ,  $\text{FeMgMnO}_x$ ,  $\text{FeMgAlO}_x$ ,  $\text{FeMgCrO}_x$ ,  $\text{FeMnAlO}_x$ ,  $\text{FeMnCrO}_x$ ,  $\text{FeAlCrO}_x$ ,  $\text{FeMnAlCrO}_x$  (MEO(-Mg)),  $\text{FeMgAlCrO}_x$  (MEO(-Mn)),  $\text{FeMgMnCrO}_x$  (MEO(-Al)),

**Table 1**

The fitting parameters of  $^{57}\text{Fe}$  Mössbauer spectra of as synthesized and cycled FO, FeMgO<sub>x</sub>, FeMgMnO<sub>x</sub>, MEO(-Cr), and HEO.

Samples	IS (mm s <sup>-1</sup> ) <sup>a</sup>	QS (mm s <sup>-1</sup> ) <sup>b</sup>	H (T) <sup>c</sup>	A (%) <sup>d</sup>	Assignment	Ref.
FO	0.35	-0.01	48.8	34.5	Fe <sup>3+</sup> - A site of spinel	[65, 66]
	0.73	0.00	45.7	59.6	Fe <sup>3+</sup> /Fe <sup>2+</sup> - B site of spinel	
FeMgO <sub>x</sub>	1.12	-	-	5.9	Fe <sup>2+</sup>	[67]
	0.25	0.00	45.2	54.0	Fe <sup>3+</sup> - A site of spinel	[68, 69]
	0.28	-0.07	42.7	34.3	Fe <sup>3+</sup> - B site of spinel	
	0.34	-0.01	48.5	8.7	Fe <sup>3+</sup> - B site of spinel	
	0.25	2.26	-	3.0	Fe <sup>3+</sup> - superparamagnetic	
	0.30	0.04	33.6	15.7	Fe <sup>3+</sup> - A site of spinel	
FeMgMnO <sub>x</sub>	0.32	0.01	30.3	22.1	Fe <sup>3+</sup> - B site of spinel	
	0.28	0.01	39.8	6.5	Fe <sup>3+</sup> - B site of spinel	
	0.28	0.02	36.8	41.7	Fe <sup>3+</sup> - A site of spinel	
	0.37	-0.02	21.6	10.8	Fe <sup>3+</sup> - B site of spinel	
	0.29	1.72	-	3.2	Fe <sup>3+</sup> - superparamagnetic	
	0.27	0.68	-	62.6	Fe <sup>3+</sup> - A site of spinel	[70, 71]
HEO	0.33	1.01	-	37.4	Fe <sup>3+</sup> - B site of spinel	
	0.41	0.77	-	53.6	Fe <sup>3+</sup> - A site of spinel	[71]
FO-C	0.37	1.05	-	46.4	Fe <sup>3+</sup> - B site of spinel	
	0.28	0.00	49.1	35.7	Fe <sup>3+</sup> - A site of spinel	[65, 66]
	0.66	0.00	46.0	64.3	Fe <sup>3+</sup> /Fe <sup>2+</sup> - B site of spinel	
FeMgO <sub>x</sub> -C	0.28	-0.03	48.4	27.0	Fe <sup>3+</sup> - A site of spinel	[68, 69, 71]
	0.31	-0.12	45.7	16.0	Fe <sup>3+</sup> - B site of spinel	
FeMgMnO <sub>x</sub> -C	0.81	0.13	45.5	20.2	Fe <sup>2+</sup>	
	1.05	0.62	-	14.8	Fe <sup>2+</sup> - rock-salt	
	1.05	0.94	-	22.0	Fe <sup>2+</sup> - rock-salt	
	0.31	0.00	52.4	5.2	Fe <sup>3+</sup> - spinel	
	0.31	0.27	-	31.4	Fe <sup>3+</sup> - spinel	
MEO(-Cr)-C	1.43	1.01	-	41.9	Fe <sup>2+</sup> - rock-salt	
	1.43	1.70	-	21.5	Fe <sup>2+</sup> - rock-salt	
	0.27	-0.01	43.1	21.2	Fe <sup>3+</sup> - A site of spinel	
HEO-C	0.34	-0.15	37.9	18.3	Fe <sup>3+</sup> - B site of spinel	
	0.31	0.78	-	38.6	Fe <sup>3+</sup>	
	0.99	1.26	-	22.0	Fe <sup>2+</sup> - rock-salt	
	0.29	0.54	-	51.3	Fe <sup>3+</sup> - A site of spinel	
	0.35	0.83	-	37.8	Fe <sup>3+</sup> - B site of spinel	
	1.63	-	-	10.9	Fe <sup>2+</sup> - B site of spinel	

<sup>a</sup>IS: isomer shift; <sup>b</sup>QS: quadrupole shift; <sup>c</sup>H: hyperfine field; <sup>d</sup>A: the ratio of the corresponding Fe species. “-C” refers to the samples after 10 cycles.

and FeMgMnAlO<sub>x</sub> (MEO(-Cr)), which have same molar ratio of each metal. The detailed process for redox material preparation is shown in Scheme 1.

## 2.2. Redox materials characterization

The PANalytical X'Pert-Pro powder x-ray diffractometer was used to investigate the powder X-ray diffraction (XRD) patterns of the samples at various stages (fresh, after reduction, and after multicycle tests) with a scanning speed of 8 degrees per minute in the range of 10–90 degree. Cu K $\alpha$  radiation (0.15432 nm) was adopted and operated at 40 kV and 40 mA.

The energy dispersive X-ray spectroscopy (EDS) element mappings and high-resolution transmission electronic microscopy (HRTEM) were

accomplished on JEOL JEM-2100 F apparatus. The morphology of fresh and reduced samples with the same oxygen converted (68.5 mL g<sup>-1</sup>) was collected by field emission scanning electron microscopy (SEM, JEOL JSM-7800 F). Raman spectra of the redox materials processed under various conditions were measured on a NanoWizard Raman spectrometer in the range of 100–1800 cm<sup>-1</sup> by 532 nm laser source. The number of the scans and the intensity of the laser could be regulated to obtain the optimal results.

To evaluate the near-surface element states, *ex-situ* X-ray photo-electron spectroscopy (XPS) measurements were carried out on Thermo Fisher Scientific ESCALAB 250Xi (Al K $\alpha$ ,  $h\nu = 1486.6$  eV) under the pressure of  $3 \times 10^{-8}$  Pa. The reduced samples were pretreated with 1 vol % CH<sub>4</sub>/Ar (100 mL min<sup>-1</sup>) for 6 min at 900 °C and then cooled down to room temperature under Ar (200 mL min<sup>-1</sup>). All the samples were pressed and transferred on the sample holder exposed in air. The binding energies of redox materials were corrected with the C 1 s peak of contaminated carbon (284.8 eV) as the internal standard. XPSPEAK software using Shirley background and Gaussian-Lorentzian functions was implemented to fit the peaks.

The  $^{57}\text{Fe}$  Mössbauer spectra were measured in constant acceleration mode using an MFD-500AV-02 spectrometer with  $^{57}\text{Co}$   $\gamma$ -quantum source confined in Rh matrix. During the tests, the content of Fe species in each sample was ensured to be around 10 mg. The reduced samples were pretreated with 1 vol% CH<sub>4</sub>/Ar (100 mL min<sup>-1</sup>) for 6 min at 900 °C and then cooled down to room temperature under Ar (200 mL min<sup>-1</sup>). Subsequently, they were transferred to a vacuum plastic bag and sealed as soon as possible to avoid extensive oxidation (within 1 min). The data of fresh and cycled (10 cycles) samples was collected under air at room temperature while the reduced samples were performed under the vacuum condition. A least-squares fitting procedure was utilized to fit the spectra via MossWinn software. The  $\alpha$ -Fe (room temperature) was employed as a reference to calibrate the isomer shifts (IS) value.

The water splitting activities of redox materials were investigated by H<sub>2</sub>O-temperature programmed surface oxidation reaction (H<sub>2</sub>O-TPSO), which were conducted on IPI GAM200 quadrupole mass spectrometer (MS). In a representative experiment, 100 mg of fresh HEO (40–60 mesh) was put into a quartz tube and heated to 900 °C at a ramp rate of 10 °C min<sup>-1</sup> under Ar atmosphere (30 mL min<sup>-1</sup>), and then 1 vol% CH<sub>4</sub>/Ar was injected into the reactor with a flow rate of 100 mL min<sup>-1</sup> for 6 min (the amount of the oxygen converted was 68.5 mL g<sup>-1</sup>), followed by cooling to 100 °C under Ar (30 mL min<sup>-1</sup>). Thereafter, TPSO analysis was performed from this temperature to 900 °C at a ramp rate of 10 °C min<sup>-1</sup> under 4.2 vol% H<sub>2</sub>O/Ar (30 mL min<sup>-1</sup>). The line for the water steam was heated to 140 °C to prevent H<sub>2</sub>O condensation. FeMgO<sub>x</sub>, MEO-(Mg), MEO-(Mn) and MEO-(Al) were pretreated separately with 1 vol% CH<sub>4</sub>/Ar (100 mL min<sup>-1</sup>) for 3 min 43 s, 7 min 6 s, 6 min 22 s, and 6 min 3 s while FO and MEO(-Cr) were processed under 8 vol % H<sub>2</sub>/Ar (30 mL min<sup>-1</sup>) for 3 min 29 s and 5 min 4 s at 900 °C, respectively, to achieve the same oxygen converted (68.5 mL g<sup>-1</sup>) before TPSO test.

*In-situ* diffuse reflectance infrared Fourier transform spectroscopy (*in-situ* DRIFTS) was performed on a Bruker EQUINOX 70 equipped with an *in-situ* cell. The signals of the gases and adsorbed species were examined by a mercury-cadmium-telluride (MCT) detector cooled by liquid N<sub>2</sub>. The reduced samples with the same oxygen converted (68.5 mL g<sup>-1</sup>) were pretreated at 400 °C for 30 min under He (30 mL min<sup>-1</sup>), and then redox materials were cooled down to 50 °C. The treatments of the reduced samples were the same as these of H<sub>2</sub>O-TPSO experiments. To prevent the changes of background and temperature-induced features, each spectrum was obtained under 50 °C by scanning 64 times from 4000 cm<sup>-1</sup> to 1000 cm<sup>-1</sup> with a resolution of 4 cm<sup>-1</sup>. Following three separate recording of the background and sample spectra, the gas was switched to 5 vol% CO/He (30 mL min<sup>-1</sup>), the spectra were recorded every 0.5 min in the first 10 min, and then the signals were collected every 2 min up to 30 min

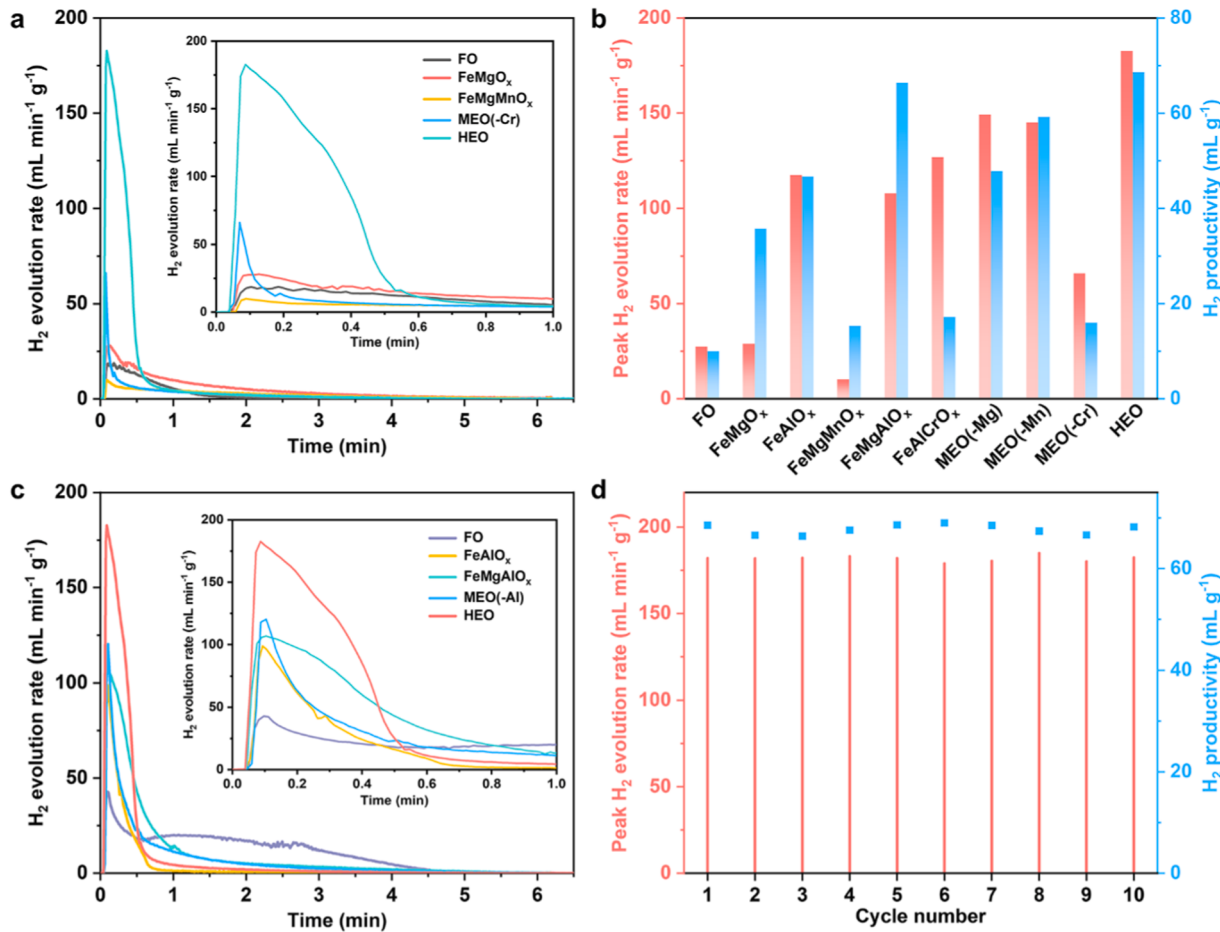


**Fig. 5.** (a) Transient H<sub>2</sub> evolution rates during water splitting step for FO, FeMgO<sub>x</sub>, FeMgMnO<sub>x</sub>, MEO(-Cr) and HEO, (b) peak H<sub>2</sub> evolution rates and total H<sub>2</sub> productivities of typical oxides, (c) transient H<sub>2</sub> evolution rates during water splitting step for FO, FeAlO<sub>x</sub>, FeMgAlO<sub>x</sub>, MEO(-Al) and HEO with the same oxygen converted (68.5 mL g<sup>-1</sup>), and (d) peak H<sub>2</sub> evolution rates and H<sub>2</sub> productivities of HEO during 10 cycles.

### 2.3. Reactivity evaluation

The reactivity evaluations of spinel oxides were assessed in a quartz tube microreactor fixed in the center of an infrared image furnace (VTH-E44, Advance Riko) under atmospheric pressure. The temperature of reaction was detected by a R-type thermocouple coated by alumina ( $\pm 3.8$  °C) in close proximity to the sample and controlled by TPC-5000. Typically, 100 mg of the sample (40–60 mesh) was loaded in a quartz tube encased by two layers of quartz wool. During the MDR step, the reactor was filled with 1 vol% CH<sub>4</sub>/Ar for 6 min (100 mL min<sup>-1</sup>). For H<sub>2</sub>O splitting reaction (STWS), water vapor (30 °C) was brought into the tube by Ar with a flow rate of 700 mL min<sup>-1</sup> (4.2 vol% H<sub>2</sub>O/Ar) to react with the reduced redox material for 6 min. Between the two steps, the residual gas from the previous stage was eliminated with Ar for 6 min (200 mL min<sup>-1</sup>). The reactions were performed at 900 °C. The line for the water steam was heated to 140 °C to prevent H<sub>2</sub>O condensation. The outlet gas concentrations were constantly monitored and quantified by MS. The linear relationship between ion current and concentration was calibrated by various standard gases before the measurement, which were close to those involved in the reaction. The *m/z* ratio of 15 was employed for CH<sub>4</sub>, *m/z* of 44 and 28 for CO<sub>2</sub>, *m/z* of 28 again for CO, *m/z* of 2 for H<sub>2</sub>, and *m/z* of 40 for Ar. The concentrations of the gases quantified by MS signals were integrated to calculate the amount of the corresponding component. The calculations of CH<sub>4</sub> conversion, CO and CO<sub>2</sub> selectivity, carbon balance, the transient H<sub>2</sub> evolution rate, and H<sub>2</sub> productivity in MDR-STWS were provided in the [Supporting information](#). Considering the measurement inaccuracy of the mass spectroscopy

detector, the carbon balance (95–105 %) of the process was considered adequate.

### 2.4. DFT calculations

Vienna ab initio simulation package (VASP) code [39] was employed to explore the first-principle calculations, which was based on the density functional theory (DFT). The electronic exchange and correlation effects were depicted by the generalized gradient approximation (GGA) with the Perdew-Burke-Ernzerhof (PBE) exchange-correlation functional [40–42]. In each case, the cutoff energy was fixed to 600 eV. In order to ensure the accuracy of the structures, structural optimization would be carried out within the energy difference less than 10<sup>-6</sup> eV until the forces less than 0.03 eV Å<sup>-1</sup>. For bulk geometry optimizations and surface geometry optimizations, their Brillouin-zone integrations were performed by Monkhorst-Pack mesh with the density of one point per  $\sim$ 0.03 Å<sup>-3</sup> (ref. [43]). For electronic structure calculations, their Brillouin-zone integrations were performed with the density of one point per  $\sim$ 0.02 Å<sup>-3</sup> (ref. [43]). An effective Hubbard U = 3.8 eV was used for Fe [44,45], 4.0 eV for Mn [46] and 3.0 eV for Cr [46]. A 15 Å vacuum layer was applied to separate the periodic models in the z-direction of the slab models. The D3 Grimme correction was adopted to consider van der Waals (vdW) interactions in all reaction processes [47]. The nudged elastic band (NEB) combined with minimum-mode following dimer method was employed to obtain the transition state structures of the reaction [48]. Moreover, the calculations were considered converged when the maximum forces on all atoms were less than 0.05 eV Å<sup>-1</sup>.

**Table 2**

The amounts of maximum theoretical oxygen, maximum theoretical hydrogen production, actual oxygen converted, oxygen conversion, and theoretical Fe species of a series of FO, binary, ternary (LEO), quaternary (MEO) and quinary (HEO) spinel oxides.

Name	Maximum theoretical oxygen or hydrogen (mL g <sup>-1</sup> ) <sup>a</sup>	Actual oxygen converted (mL g <sup>-1</sup> ) <sup>b</sup>	Oxygen conversion (%) <sup>c</sup>	Theoretical Fe species (wt %) <sup>d</sup>
FO	435.4	18.9	4.3	72.4
FeMgO <sub>x</sub>	273.6	89.3	32.6	45.5
FeMnO <sub>x</sub>	211.6	81.1	38.3	35.2
FeAlO <sub>x</sub>	256.8	94.8	36.9	42.7
FeCrO <sub>x</sub>	215.6	79.9	37.1	35.8
FeMgMnO <sub>x</sub>	168.8	60.6	35.9	28.1
FeMnAlO <sub>x</sub>	160.2	43.3	27.0	26.6
FeMgAlO <sub>x</sub>	196.3	65.9	33.6	32.6
FeMgCrO <sub>x</sub>	171.3	63.2	36.9	28.5
FeMnCrO <sub>x</sub>	148.2	29.6	20.0	24.6
FeAlCrO <sub>x</sub>	162.5	59.5	36.6	27.0
MEO(-Mg)	122.1	59.1	48.4	20.3
MEO(-Mn)	137.4	61.3	44.6	22.8
MEO(-Al)	123.3	65.4	53.1	20.5
MEO(-Cr)	135.8	26.1	19.2	22.6
HEO	109.5	68.5	62.6	18.2

<sup>a</sup> The maximum theoretical oxygen =  $3 \times \frac{1}{M} \times x \times 1000 \times 0.5 \times 22.4$ , where M indicates the molar weight of redox material, x represents the atomic ratio of Fe species in the redox material. The maximum theoretical oxygen was calculated based on the complete conversion of Fe<sup>3+</sup> to Fe<sup>0</sup> considering the results of XPS and <sup>57</sup>Fe Mössbauer spectroscopy that the oxidation states of Mn and Cr species did not change greatly after reduction (Fig. S6) and the reduction of Fe species principally contributed to the oxygen converted (Fig. S7 and Table S3). The maximum theoretical hydrogen production was equal to the maximum theoretical oxygen.

<sup>b</sup> The actual oxygen converted was calculated by the [Equation 6 in the Supporting information](#).

$$\text{Oxygen conversion} = \frac{\text{actual converted oxygen}}{\text{theoretical oxygen}} \times 100\%.$$

<sup>c</sup> The weight% of theoretical Fe species =  $\frac{M_{\text{Fe}}}{M} \times 100\%$ , where M indicates the molar weight of redox material, M<sub>Fe</sub> represents the molar weight of Fe species of redox material.

Meanwhile, the transition states were verified using a single imaginary frequency.

During the calculations of H<sub>2</sub>O activation, we used FeO to simplify calculations on the rock salt oxides produced by the reduction of most LEO and MEO samples, due to the complexity and inconsistency of their structural compositions. Fe(110) was chosen to simulate the Fe<sup>0</sup> nanoparticles generated by the reduction of part LEO, MEO and HEO. In addition, Fe<sup>0</sup>/HEO(311) with oxygen vacancy (Fe<sup>0</sup>/HEO) was adopted to calculate the abundant interfacial sites of reduced HEO, resulting from the smaller Fe<sup>0</sup> nanoparticles. FeO(001) and Fe(110) were constructed by a p(1 × 1) cell of 2 × 2 × 2 supercell and a p(2 × 2) supercell with five layers, respectively. A p(1 × 1) slab model was constructed based on a series of characterizations (including XRD and <sup>57</sup>Fe Mössbauer spectroscopy) and previous research [49] to simulate HEO. These surface models were optimized and presented in Fig. S1. The other details about DFT calculation and adsorption models are provided in the [Supporting information](#).

### 3. Results and discussions

#### 3.1. The formation of high-entropy spinel oxide

X-ray diffraction (XRD) characterizations of different spinel oxides containing one to five metal species were conducted to clarify their

structure. As shown in Fig. 1, various impurities such as MgO, Al<sub>2</sub>O<sub>3</sub>, hematite, bixbyite, eskolaite, and secondary spinel oxides besides primary spinel phase could be observed in the most binary, ternary (LEO), and quaternary (MEO) oxides, which was further confirmed by EDS mapping wherein metal atoms distributed inhomogeneously (Fig. 2b-d and Fig. S2). With the increase of metal species, only single-phase spinel could be detected in the HEO (Fig. 1a). Moreover, its EDS mapping result also showed that the elements distributed uniformly (Fig. 2e). This should be due to the enhancement of entropic contribution effectively counteracting the mixing enthalpy ( $\Delta G_{\text{mix}} = \Delta H_{\text{mix}} - T\Delta S_{\text{mix}}$ ) and thus favorable for the formation of a uniform structure.

Raman spectra of fresh samples at room-temperature were recorded in the range of 100–1800 cm<sup>-1</sup>, as shown in Fig. 3. Three modes of A<sub>1g</sub>, E<sub>g</sub>, and T<sub>2g</sub> were observed in all the fresh samples based on the fact that they are inverse-like spinel structures belonging to the Fd<sub>3</sub>m space group [50]. In addition, it could be found that the width of peak locating at around 720 cm<sup>-1</sup> with a shoulder at around 650 cm<sup>-1</sup> gradually increased with the metal species and tended to a large bulge peak, which was caused by increased disorder of samples [51,52]. It was considered that the disorder of spinel related with the proportion of Fe in the A sites in the all elements of A sites (tetrahedral sites) (Fe in the A sites/A). Consequently, <sup>57</sup>Fe Mössbauer spectroscopy was employed to investigate the coordination environment of Fe cations to describe the disorder quantitatively. For Fe<sub>3</sub>O<sub>4</sub>, two sextets could be observed, which were attributed to Fe<sup>3+</sup>(Fe<sup>2+</sup>) in tetrahedral (A) and octahedral (B) sites, respectively (Fig. 4a and Table 1). In addition, a singlet was also seen which was ascribed to Fe<sup>2+</sup> due to the Ar atmosphere during calcination leading to the reduction of partial FeO<sub>x</sub> species. With the increase of doped metals, Fe<sup>3+</sup> in these two positions exhibited more types of hyperfine field responses, which was due to different chemical environment of Fe cations (number of surrounding metal atoms differs). Moreover, the superparamagnetic Fe<sup>3+</sup> species appeared accompanied with complete disappearance of sextets when the number of doped metals is larger than 3, which might be because more metals incorporating into spinel increased the mean distance of neighboring magnetic Fe<sup>3+</sup> thereby decreasing the magnetic hyperfine interaction. It was worthwhile to note that the ratio of Fe in the A sites/A decreased progressively with the increase in the number of doped metals and the value dropped to about 32.2 % for HEO sample which was close to the theoretical value of complete mixing of 25 % (Fig. 4b and Table S1), indicating that HEO should be formed. To be summarized, we successfully designed and prepared a HEO with exclusively spinel structure.

#### 3.2. Redox performance and stability

Fig. 5 shows the performances of H<sub>2</sub>O splitting of a series of LEO, MEO and HEO spinel oxides after isothermal CH<sub>4</sub> reduction. It can be seen that the peak H<sub>2</sub> production rates and total productivities of HEO were much higher than other LEO and MEO, and they reached 182.9 mL min<sup>-1</sup> g<sup>-1</sup> and 68.5 mL g<sup>-1</sup> (Fig. 5a and b), respectively, which were several times higher than those of the spinels reported [11,29,37] and also superior to those of state-of-the-art materials [9,17] for H<sub>2</sub>O splitting (Table S2). It was noted that the amount of oxygen converted differed greatly (Table 2) for these samples (FO, FeMgMnO<sub>x</sub>, FeMnAlO<sub>x</sub>, MEO(-Mg) and MEO(-Cr), et al.) during CH<sub>4</sub> reduction, which gave rise to distinct oxygen vacancies for H<sub>2</sub>O splitting. To further disclose the impact of entropy on H<sub>2</sub>O splitting performance, H<sub>2</sub>O splitting reactivity of HEO and some reference samples after subjected into 8 vol% H<sub>2</sub>/Ar or 1 vol% CH<sub>4</sub>/Ar for different time at 900 °C to reach the same lattice oxygen converted were evaluated under the identical operating conditions. As shown in Fig. 5c, the peak H<sub>2</sub> production rate of HEO still far exceeded that of LEO and MEO, indicating the high-entropy oxide can accelerate the H<sub>2</sub>O splitting process, which might originate from the metal/HEO interfaces more favorable for H<sub>2</sub>O activation. On the other hand, HEO also exhibited better reactivity than most LEO and MEO did

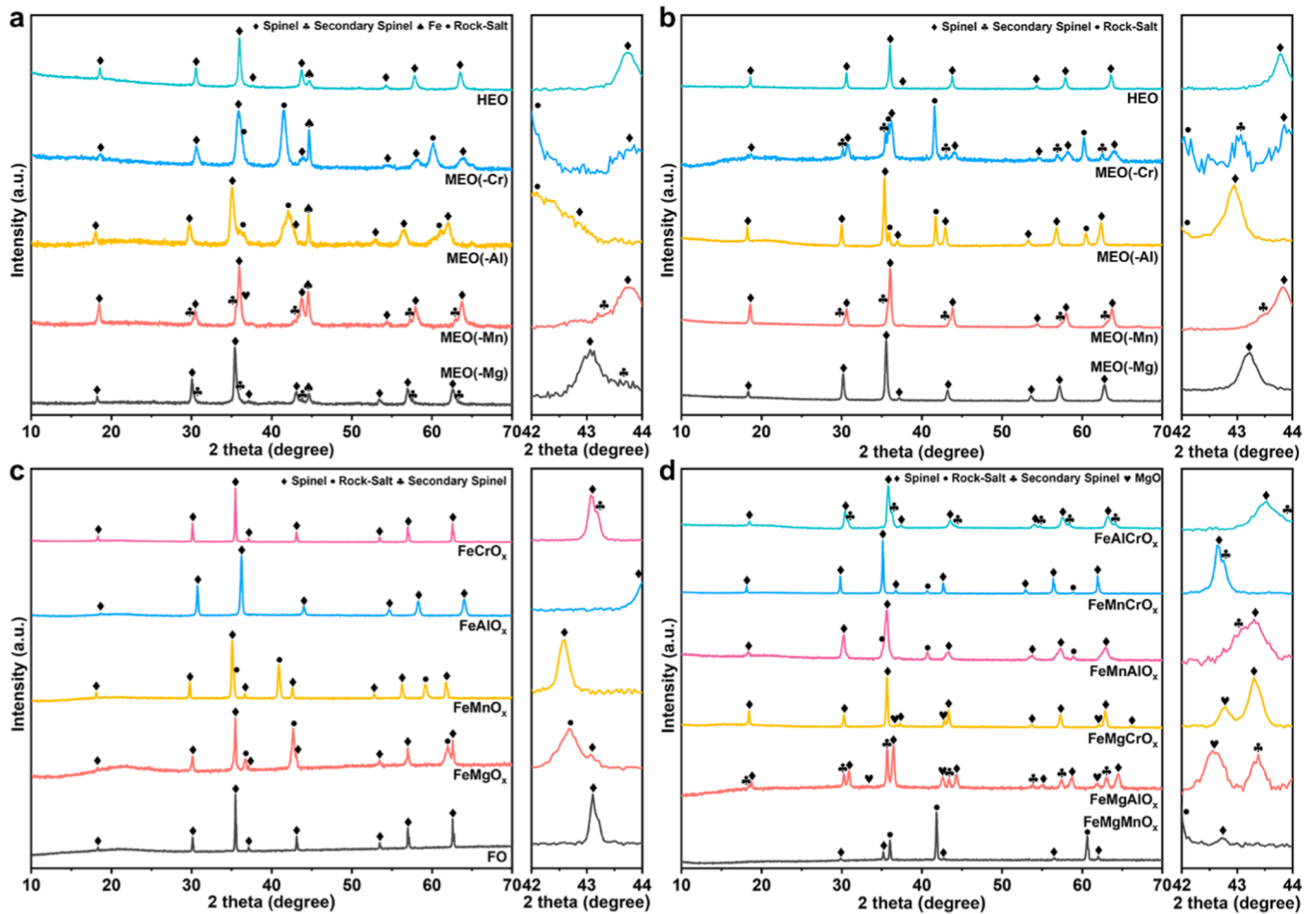


**Fig. 6.** XRD patterns of (a) reduced MEOs and HEO (same oxygen converted, 68.5 mL g<sup>-1</sup>), (b) cycled MEOs and HEO, (c) cycled FO and binary oxides, (d) cycled ternary oxides, and their corresponding magnified views in the range of 42–44 degree (2 theta). The cycled samples refer to those after 10 cycles.

during the 2nd CH<sub>4</sub> reduction with conversion of larger than 88 %, CO selectivity of about 90 % and H<sub>2</sub>/CO of 2 nearly without carbon deposition (Fig. S3), demonstrating superior performance of HEO to that of other binary, ternary and quaternary spinel oxides for MDR-STWS.

Fig. 5d and Fig. S4 show the stability results of HEO in MDR-STWS and that of other spinel oxides were also presented in Fig. S5. It could be observed that peak H<sub>2</sub> evolution rate of around 180 mL min<sup>-1</sup> g<sup>-1</sup> and productivity of about 70 mL g<sup>-1</sup> were almost identical for HEO whereas they were lower and decreased with distinct extent for other LEO and MEO during 10 redox cycles, indicating that HEO exhibited not only higher performance but also better stability in MDR-STWS. It was reported that the amount of oxygen converted of oxides had to be carefully controlled (usually < 30 mL g<sup>-1</sup>) to alleviate the degradation of performance with redox cycles thus leading to inferior hydrogen productivity and overall process efficiency [28,53–57]. In the present work, the amount of oxygen converted reached almost 70 mL g<sup>-1</sup> with oxygen conversion degree exceeding 60 % (Table 2. The detail of calculation was shown in Fig. S6, Fig. S7 and Table S3 in the Supporting information) and stable performance could still be achieved for HEO, demonstrating its extraordinary H<sub>2</sub>O splitting performance, which rendered it highly promising in MDR-STWS process.

### 3.3. Redox materials characterization

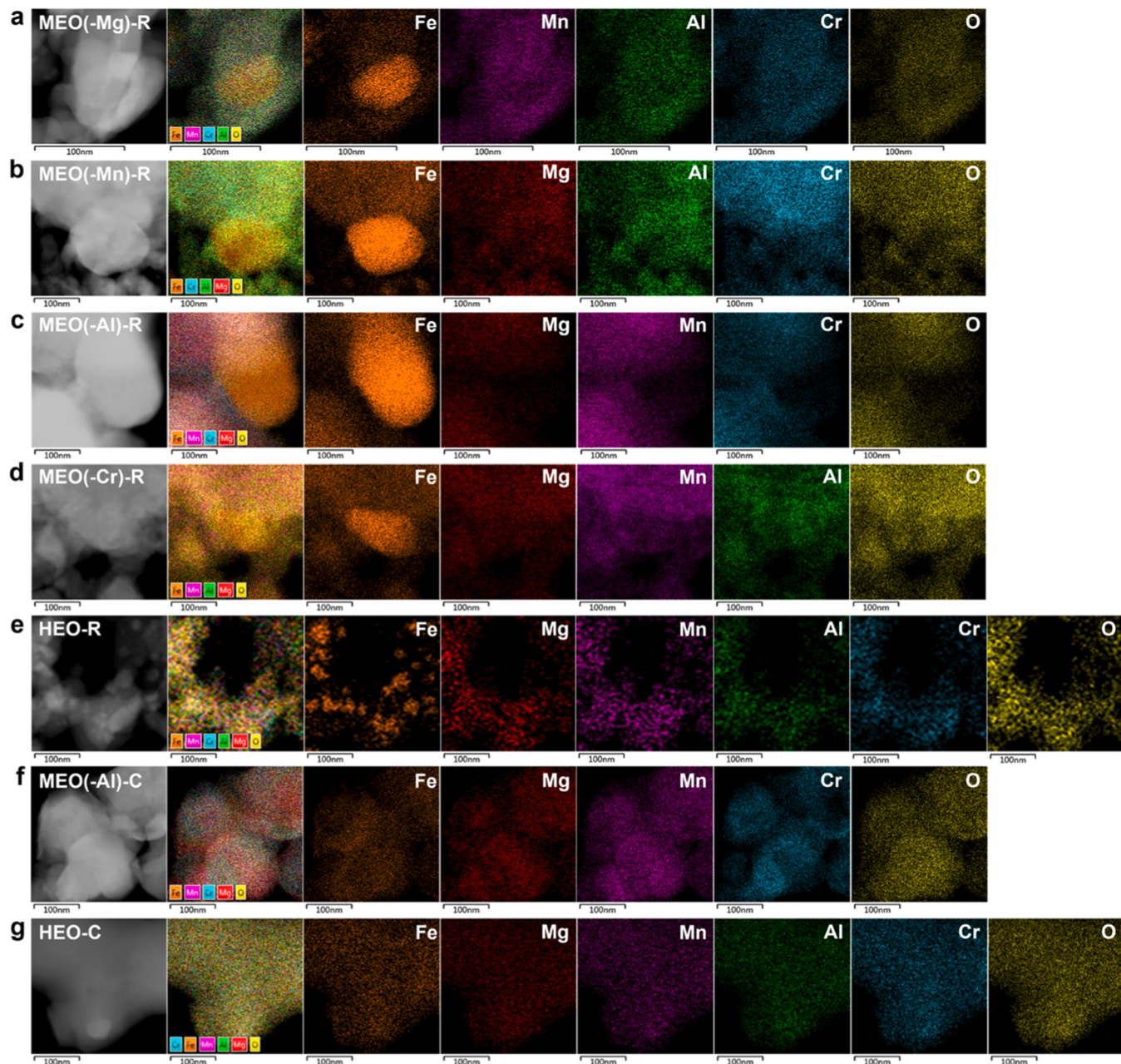
#### 3.3.1. Reduced samples

Fig. 6a shows X-ray diffraction patterns of reduced HEO (HEO-R) and MEO (MEO-R) reference samples for different time (6 min for HEO, 5 min 4 s for MEO(-Cr), 6 min 3 s for MEO(-Al), 6 min 22 s for MEO

(-Mn) and 7 min 6 s for MEO(-Mg)) with the same amount of oxygen converted (68.5 mL g<sup>-1</sup>) considering their better performance than LEO for MDR-STWS. It should be noted that the additional sintering could not be observed for the sample reduced for longer time (Fig. S8a-d). It could be seen that the spinel phase was still observed accompanied by a new diffraction peak assigned to Fe<sup>0</sup> for HEO-R [58]. In addition, no secondary phases were found such as the rock-salt, indicating that the spinel structure could be maintained even at large amount of oxygen converted (about 70 mL g<sup>-1</sup>) for HEO. In comparison, rock-salt structure was found besides spinel and Fe<sup>0</sup> for all the MEO-R samples, suggesting the destruction of spinel structure after reduction. It was worthwhile to note that the peak width and intensity of Fe<sup>0</sup> in HEO-R was significantly wider and lower than those in MEO-R, which indicated smaller crystal size (Table S4). This could be further demonstrated by EDS mapping results in which the size of the Fe<sup>0</sup> nanoparticle was about 20–30 nm in HEO-R, greatly lower than that in MEO-R with particle size of larger than 100 nm (Fig. 7a-e). It was reported that exsolved metal nanoparticles usually sintered severely particularly under extensive amount of oxygen converted, which was caused by the destruction of host structure [25,27,58]. Our HEO preserved spinel structure with the amount of oxygen converted of about 70 mL g<sup>-1</sup> driven by entropy, remarkably enhancing the stability of substantial exsolved Fe<sup>0</sup> nanoparticles, which would give rise to abundant interfaces between Fe<sup>0</sup> and HEO as active sites for H<sub>2</sub>O activation.

#### 3.3.2. Cycled samples

Fig. 6b-d show X-ray diffraction patterns of cycled HEO (HEO-C), LEO-C, and MEO-C reference samples. Only spinel phase was observed



**Fig. 7.** EDS element mappings of reduced (a) MEO(-Mg), (b) MEO(-Mn), (c) MEO(-Al), (d) MEO(-Cr), and (e) HEO with the same oxygen converted ( $68.5 \text{ mL g}^{-1}$ ), and cycled (f) MEO(-Al) and (g) HEO. “MEO(-Al)-C” and “HEO-C” refer to MEO(-Al) and HEO after 10 cycles, respectively.

without metallic Fe, iron oxides, and rock-salt in HEO-C with uniformly distributed elements (Fig. 7g) and it had good crystallinity and no obvious amorphous structures were found (Fig. S8e and f), indicating extraordinary structure stability of HEO during MDR-STWS process. However, rock-salt structure and other oxides besides single-phase spinel were found in the most LEO-C and MEO-C samples with unevenly distributed elements (Fig. 6b-d and Fig. 7f). The Raman spectroscopy results of HEO-C showed that the peaks of  $A_{1g}$  and  $T_{2g}$  of the spinel structure hardly changed compared with those in fresh HEO (Fig. S9), indicating that high disorder was still maintained for HEO after multiple redox cycles. XPS results presented that the proportion of  $\text{Fe}^{3+}$  at octahedral and tetrahedral sites [57,59] in HEO-C was similar to that in fresh HEO (Fig. S6l and Table S5) although subtle amount of  $\text{Fe}^{2+}$  was detected, which should be due to the increased oxygen vacancies (Fig. S6l and Table S5). In addition, the peaks centered at 641.5 and 577.1 eV could be attributed to the  $2p_{3/2}$  of  $\text{Mn}^{3+}$  and  $\text{Cr}^{3+}$ , respectively

[59,60], also did not change after 10 cycles (Fig. S6l). These results indicated that the chemical environment of metal cations in HEO-C did not change greatly during the reaction process. Similar results were also obtained in  $^{57}\text{Fe}$  Mössbauer spectroscopy in which the amount of  $\text{Fe}^{3+}$  in tetrahedral and octahedral sites after 10 cycles was almost the same to that in fresh HEO (Fig. 4a and c and Table 1). Moreover, the content of Fe in A site in fresh HEO was similar to that in HEO-C (32.2 % vs. 31.0 % in Table S1), which was close to the theoretical value when it was completely uniformly distributed, indicating that the sample after 10 cycles was highly chaotic and high-entropy was conducive to the stability of its structure. However, large amount of  $\text{Fe}^{2+}$  in rock-salt structure besides  $\text{Fe}^{3+}$  in spinel in LEO-C and MEO-C was detected (Fig. 4c and Table 1), pointing toward that the spinel structures were destroyed during multiple redox cycles of MDR-STWS, as state-of-the-art spinel oxides suffered from. The high-entropy effect in HEO was more favorable to form a single-phase metal oxide due to lower Gibbs free

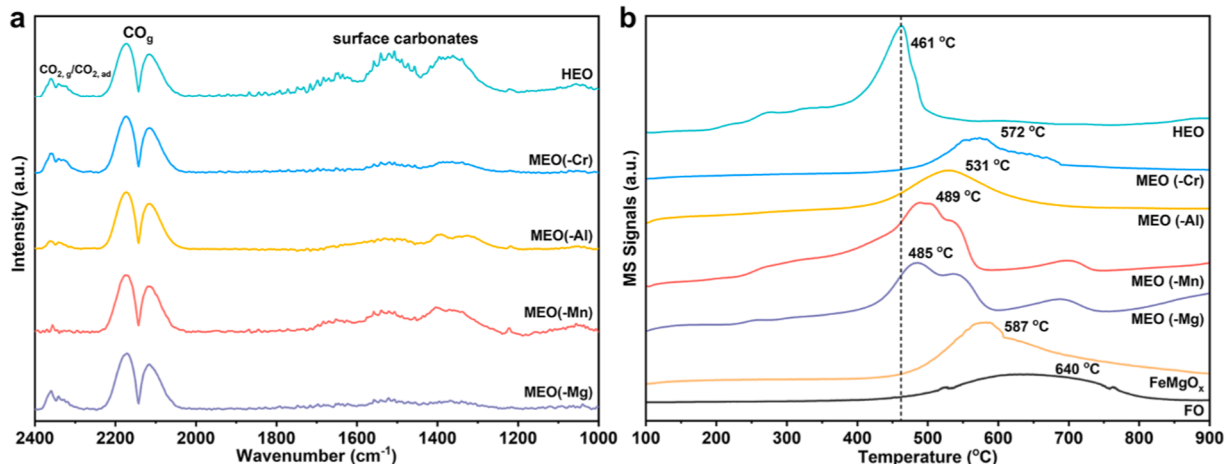


**Fig. 8.** (a) In-situ CO DRIFTS of reduced MEO(-Mg), MEO(-Mn), MEO(-Al), MEO(-Cr) and HEO and (b) H<sub>2</sub>O-TPSO characterizations of reduced FO, FeMgO<sub>x</sub>, MEO(-Mg), MEO(-Mn), MEO(-Al), MEO(-Cr) and HEO. All of the reduced samples have the same amount of oxygen converted (68.5 mL g<sup>-1</sup>). “CO<sub>2,g</sub>”, CO<sub>2,ad</sub>, and “CO<sub>g</sub>” refer to the signals of gaseous CO<sub>2</sub>, adsorbed CO<sub>2</sub>, and gaseous CO, respectively.

energy, which promoted lots of exsolved Fe<sup>0</sup> nanoparticles with the amount of oxygen converted of about 70 mL g<sup>-1</sup> back into the host spinel structure and then accounting for the extraordinary stability of HEO in MDR-STWS.

### 3.3.3. Fe<sup>0</sup>/HEO interfaces with metal-oxygen vacancy pairs for H<sub>2</sub>O activation

It has been reported that the amount of oxygen converted of oxide materials must be manipulated carefully (< 30 mL g<sup>-1</sup>) in order to prevent the host matrix from destruction inducing the sintering of exsolved nanoparticles and difficulty in its reintegrating into the host structure, which brought about inferior H<sub>2</sub> production rate and productivity for MDR-STWS, just as the most LEO and MEO showed (Fig. 4c, Fig. 5a–c, Fig. 6, and Fig. 7). In this work, high-entropy spinel oxide achieved superior performance of H<sub>2</sub>O splitting to the state-of-the-art materials. This should be attributed to the motivation by entropy effect maintaining spinel structure at large amount of oxygen converted (almost 70 mL g<sup>-1</sup>) thereby stabilizing plenty of exsolved Fe<sup>0</sup> nanoparticles (Fig. 6a, Fig. 7e and Table 2), which gave rise to abundant Fe<sup>0</sup>/HEO interfaces with more metal-oxygen vacancy pairs facile to H<sub>2</sub>O activation. Indeed, in-situ CO adsorbed DRIFTS experiments of the reduced samples with the same amount of lattice oxygen converted (68.5 mL g<sup>-1</sup>) showed that larger amount of carbonate species originating from the adsorption and activation of CO on the oxygen vacancies [61,62] generated in the reduced HEO compared with other reduced MEO (Fig. 8a), indicating that more oxygen vacancies in the Fe<sup>0</sup>/HEO interfaces were present in the reduced HEO. Furthermore, H<sub>2</sub>O-TPSO characterizations of the reduced samples with same oxygen converted (68.5 mL g<sup>-1</sup>) demonstrated that reduced HEO could significantly lower the temperature for the peak of H<sub>2</sub> evolution the most by almost 200 °C from 640 °C (FO) down to 460 °C (Fig. 8b). These results provided strong evidences that abundant Fe<sup>0</sup>/HEO interfaces with more metal-oxygen vacancy pairs in HEO were favorable for H<sub>2</sub>O activation and splitting.

DFT calculations were employed to further explain why Fe<sup>0</sup>/HEO interface with metal-oxygen vacancy pair was more preferential for H<sub>2</sub>O splitting. For simplification, we used HEO with oxygen vacancies and Fe nanowire, ideal FeO(001) and Fe(110) slab to simulate the surface structures of reduced HEO, MEO and LEO, respectively, based on the EDS mapping, XRD and <sup>57</sup>Fe Mössbauer spectroscopy results of reduced samples that small Fe<sup>0</sup> nanoparticles (about 20 nm) existed on HEO while Fe<sup>2+</sup> and large Fe<sup>0</sup> nanoparticles (about 100 nm) were present on reduced MEO and LEO (Fig. 7a–e, Fig. S7 and Table S3). As shown in Fig. 9a, the H<sub>2</sub>O splitting on Fe<sup>0</sup>/HEO interfaces with metal-oxygen vacancy pairs were more exothermic (-2.01 eV vs. 1.90 eV and

-1.52 eV) with lower activation energy (0.70 eV vs. 2.62 eV and 1.21 eV) than that on FeO(001) and Fe(110) slab (the optimized structures were shown in Figs. S10–12), disclosing that the Fe<sup>0</sup>/HEO interfaces with metal-oxygen vacancy pairs were more preferential for H<sub>2</sub>O splitting. This could be also confirmed by Bader charge analysis wherein only 0.01 e and 0.05 e transfer occurred between rock-salt FeO (001), Fe(110) and water molecule making them difficult to activate H<sub>2</sub>O by the weak interaction (Fig. 9b and c) whereas the charge changed significantly in the interfacial metal-oxygen vacancy pair of Fe<sup>0</sup>/HEO (0.29 e) decorated with H<sub>2</sub>O molecule (Fig. 9d). Moreover, the PDOS changed significantly with obvious hybridization interaction between O 2p and H 1s orbitals of H<sub>2</sub>O and all elements of Fe<sup>0</sup>/HEO especially for Fe 3d, Cr 3d and O 2p after H<sub>2</sub>O molecule adsorbed on the interface of Fe<sup>0</sup>/HEO (Fig. 9e and f), which confirmed that the metal-oxygen vacancy pairs in Fe<sup>0</sup>/HEO interfaces were beneficial to H<sub>2</sub>O activation and splitting. The high entropy effect was conducive to the maintenance of spinel structure even at large amount of oxygen converted facilitating the stabilization of substantial exsolved Fe<sup>0</sup> nanoparticles from HEO, which resulted in abundant Fe<sup>0</sup>/HEO interfaces with more metal-oxygen vacancy pairs for H<sub>2</sub>O activation and splitting by decreased reaction energy barrier and increased electronic interaction. Furthermore, entropy motivation was favorable for the recovery of lattice oxygen (Fig. S13) due to lower Gibbs energy, which drove exsolved Fe<sup>0</sup> to incorporate into the host spinel structure more easily. As a result, the extraordinary performance of HEO was achieved in multiple redox cycles of the MDR-STWS process.

## 4. Conclusions

In summary, a high-entropy spinel was designed and prepared to enhance the efficiency of two-step solar thermochemical water splitting reaction, achieving a peak H<sub>2</sub> evolution rate of 182.9 mL min<sup>-1</sup> g<sup>-1</sup> and total H<sub>2</sub> productivity of 68.5 mL g<sup>-1</sup> with nearly 100 % purity and excellent stability during multiple redox cycles, much better than other LEO and MEO as well as the most metal oxides reported in the previous work. This originated from the entropy effect maintaining spinel structure even at extensive amount of oxygen converted (about 70 mL g<sup>-1</sup>) and thus stabilizing massive exsolved Fe<sup>0</sup> from HEO, which brought about abundant Fe<sup>0</sup>/HEO interfaces with more metal-oxygen vacancy pairs to promote H<sub>2</sub>O activation and splitting by significantly lowering the barrier and enhancing electronic interaction. At the same time, high entropy effect was beneficial to the recovery of lattice oxygen as a result of lower Gibbs energy, promoting substantial exsolved Fe<sup>0</sup> metal nanoparticles to enter the bulk to form single-phase spinel structure

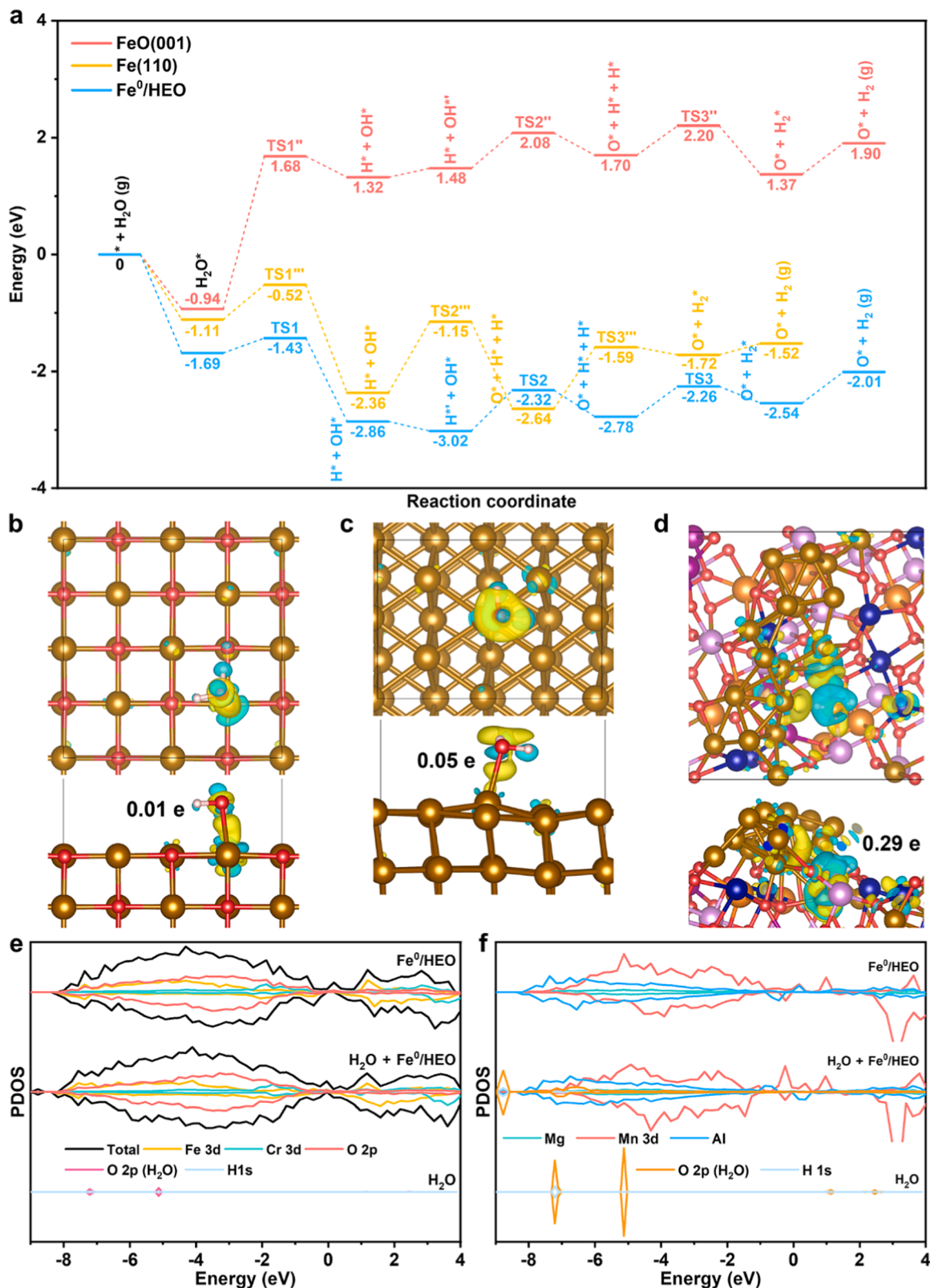


**Fig. 9.** DFT calculations. (a) Comparison of energy profiles of H<sub>2</sub>O splitting over Fe<sup>0</sup>/HEO, FeO(001) and Fe(110). “TS” stands for the dissociation transition state. Charge densities of H<sub>2</sub>O adsorption on (b) FeO(001), (c) Fe(110), and (d) the metal-oxygen vacancy pair of Fe<sup>0</sup>/HEO. The internal number represents the electron changes after H<sub>2</sub>O adsorption. The yellow and cyan distributions correspond to charge accumulation and depletion with an isosurface value of 0.005 e Å<sup>-3</sup>, respectively. ● Fe, ○ Mg, ▲ Mn, ● Al, ● Cr, ● O, ● H. (e) Projected density of states (PDOS) and (f) their magnified views of H<sub>2</sub>O molecule, Fe<sup>0</sup>/HEO, and the interaction within the H<sub>2</sub>O chemisorption on the interface with metal-oxygen vacancy pair of Fe<sup>0</sup>/HEO. Fermi level of the support is removed to 0 eV. In (e), the PDOS of Mg, Mn, and Al are not shown, and the (f) is the magnified views of the elements not shown in (e). All of the optimized structures are listed in the Supporting information (Figs. S10–12).

thereby improving the efficiency of water splitting. In contrast, severe sintering of Fe<sup>0</sup> nanoparticles and destruction of spinel structure occurred on LEO and MEO, which was responsible for lower and progressively decreased H<sub>2</sub>O splitting performance during many redox cycles of MDR-STWS. The present work proposed a strategy to enhance the performance of water splitting by considering entropic contribution for fast kinetics and stabilization of redox material, and more unique materials for metal oxides catalysis would be inspired in the near future.

### CRediT authorship contribution statement

**Yujia Han:** Sample synthesis, Experiment design, Exploration, DFT calculations, Data analysis, Writing & editing. **Ming Tian:** Writing – review & editing. **Chaojie Wang:** Experiment design, Data analysis. **Teng Zong:** Experiment design, Data analysis. **Xiaodong Wang:** Supervision, Writing – review & editing.

### Declaration of Competing Interest

The authors declare that they have no known competing financial interests or personal relationships that could have appeared to influence the work reported in this paper.

### Data availability

No data was used for the research described in the article.

### Acknowledgements

This work was supported by the National Natural Science Foundation of China (NSFC) grants (22178337). The authors sincerely thank Yang Su for his contribution to EDS element mapping characterization.

### Appendix A. Supporting information

Supplementary data associated with this article can be found in the online version at [doi:10.1016/j.apcatb.2023.123096](https://doi.org/10.1016/j.apcatb.2023.123096).

### References

- [1] A.J. Carrillo, J. Gonzalez-Aguilar, M. Romero, J.M. Coronado, Solar energy on demand: a review on high temperature thermochemical heat storage systems and materials, Chem. Rev. 119 (2019) 4777–4816, <https://doi.org/10.1021/acs.chemrev.8b00315>.
- [2] R. Schappi, D. Rutz, F. Dahler, A. Muroyama, P. Haueter, J. Lilliestam, A. Patt, P. Furler, A. Steinfeld, Drop-in fuels from sunlight and air, Nature 601 (2022) 63–68, <https://doi.org/10.1038/s41586-021-04174-y>.
- [3] Y.F. Zhao, W. Gao, S.W. Li, G.R. Williams, A.H. Mahadi, D. Ma, Solar-versus thermal-driven catalysis for energy conversion, Joule 3 (2019) 920–937, <https://doi.org/10.1016/j.joule.2019.03.003>.
- [4] N.S. Lewis, Research opportunities to advance solar energy utilization, Science 351 (2016), aad1920, <https://doi.org/10.1126/science.aad1920>.
- [5] S. Zoller, E. Koepf, D. Nizamian, M. Stephan, A. Patane, P. Haueter, M. Romero, J. Gonzalez-Aguilar, D. Liefink, E. de Wit, S. Bredelberger, A. Sizmann, A. Steinfeld, A solar tower fuel plant for the thermochemical production of kerosene from H<sub>2</sub>O and CO<sub>2</sub>, Joule 6 (2022) 1606–1616, <https://doi.org/10.1016/j.joule.2022.06.012>.
- [6] T. Kodama, High-temperature solar chemistry for converting solar heat to chemical fuels, Prog. Energy Combust. Sci. 29 (2003) 567–597, [https://doi.org/10.1016/s0360-1285\(03\)00059-5](https://doi.org/10.1016/s0360-1285(03)00059-5).
- [7] I. Staffell, D. Scamman, A.V. Abad, P. Balcombe, P.E. Dodds, P. Ekins, N. Shah, K. R. Ward, The role of hydrogen and fuel cells in the global energy system, Energy Environ. Sci. 12 (2019) 463–491, <https://doi.org/10.1039/c8ee01157e>.
- [8] J.A. Herron, J. Kim, A.A. Upadhye, G.W. Huber, C.T. Maravelias, A general framework for the assessment of solar fuel technologies, Energy Environ. Sci. 8 (2015) 126–157, <https://doi.org/10.1039/c4ee01958j>.
- [9] C.Y. Ruan, Z.Q. Huang, J. Lin, L. Li, X.Y. Liu, M. Tian, C.D. Huang, C.R. Chang, J. Li, X.D. Wang, Synergy of the catalytic activation on Ni and the CeO<sub>2</sub>-TiO<sub>2</sub>/Ce<sub>2</sub>Ti<sub>2</sub>O<sub>7</sub> stoichiometric redox cycle for dramatically enhanced solar fuel production, Energy Environ. Sci. 12 (2019) 767–779, <https://doi.org/10.1039/c8ee03069c>.
- [10] W.C. Chueh, C. Falter, M. Abbott, D. Scipio, P. Furler, S.M. Haile, A. Steinfeld, High-flux solar-driven thermochemical dissociation of CO<sub>2</sub> and H<sub>2</sub>O using nonstoichiometric ceria, Science 330 (2010) 1797–1801, <https://doi.org/10.1126/science.1197834>.
- [11] C.L. Muzychuk, B.W. Evanko, K.C. Weston, P. Lichty, X. Liang, J. Martinek, C. B. Musgrave, A.W. Weimer, Efficient generation of H<sub>2</sub> by splitting water with an isothermal redox cycle, Science 341 (2013) 540–542, <https://doi.org/10.1126/science.1239454>.
- [12] M. Pein, L. Matzel, L. Oliveira, G. Alkan, A. Francke, P. Mechnik, C. Agrafiotis, M. Roeb, C. Sattler, Reticulated porous perovskite structures for thermochemical solar energy storage, Adv. Energy Mater. 12 (2022), <https://doi.org/10.1002/aenm.202102882>.
- [13] F. Jin, C. Xu, H. Yu, X. Xia, F. Ye, X. Li, X. Du, Y. Yang, CaCo0.05Mn0.95O3-delta: a promising perovskite solid solution for solar thermochemical energy storage, ACS Appl. Mater. Interfaces 13 (2021) 3856–3866, <https://doi.org/10.1021/acsmami.0c18207>.
- [14] Y. Han, M. Tian, C. Wang, Y. Kang, L. Kang, Y. Su, C. Huang, T. Zong, J. Lin, B. Hou, X. Pan, X. Wang, Highly active and anticoke Ni/CeO<sub>2</sub> with ultralow Ni loading in chemical looping dry reforming via the strong metal-support interaction, ACS Sustain. Chem. Eng. 9 (2021) 17276–17288, <https://doi.org/10.1021/acssuschemeng.1c06079>.
- [15] A. Riaz, M.U. Ali, T.G. Enge, T. Tsuzuki, A. Lowe, W. Lipinski, Concentration-dependent solar thermochemical CO<sub>2</sub>/H<sub>2</sub>O splitting performance by vanadia-ceria multiphase metal oxide systems, Research 2020 (2020) 3049534, <https://doi.org/10.34133/2020/3049534>.
- [16] A. Riaz, W. Lipiński, A. Lowe, Cyclic oxygen exchange capacity of Ce-doped V<sub>2</sub>O<sub>5</sub> materials for syngas production via high-temperature thermochemical-looping reforming of methane, RSC Adv. 11 (2021) 23095–23104, <https://doi.org/10.1039/d1ra02234b>.
- [17] S. Chuayboon, S. Abanades, S. Rodat, Syngas production via solar-driven chemical looping methane reforming from redox cycling of ceria porous foam in a volumetric solar reactor, Chem. Eng. J. 356 (2019) 756–770, <https://doi.org/10.1016/j.cej.2018.09.072>.
- [18] A. Riaz, F. Kremer, T. Kim, S. Sattayaporn, T. Tsuzuki, W. Lipiński, A. Lowe, Experimental demonstration of vanadium-doped nanostructured ceria for enhanced solar thermochemical syngas production, Nano Energy 81 (2021), <https://doi.org/10.1016/j.nanoen.2020.105639>.
- [19] A. Riaz, M.U. Ali, W. Lipiński, A. Lowe, Enhanced oxygen exchange capacity in nano-structured vanadia–ceria multi-phase oxygen carriers for solar thermal fuel production, J. Mater. Chem. A 7 (2019) 27347–27360, <https://doi.org/10.1039/c9ta06471k>.
- [20] Z.P. Chen, Q.Q. Jiang, H.Y. An, J. Zhang, S.Q. Hao, X.J. Li, L.L. Cai, W.G. Yu, K. Y. You, X.F. Zhu, C. Li, Platinum group metal catalyst (RuO<sub>x</sub>, PtO<sub>x</sub>, and IrO<sub>x</sub>)-decorated ceria-zirconia solid solution as high active oxygen carriers for solar thermochemical CO<sub>2</sub> splitting, ACS Catal. 12 (2022) 7719–7736, <https://doi.org/10.1021/acscatal.2c02044>.
- [21] V.P. Haribal, X. Wang, R. Dudek, C. Paulus, B. Turk, R. Gupta, F. Li, Modified ceria for “low-temperature” CO<sub>2</sub> utilization: a chemical looping route to exploit industrial waste heat, Adv. Energy Mater. 9 (2019), 1901963, <https://doi.org/10.1002/aenm.201901963>.
- [22] D. Hosseini, P.M. Abdala, F. Donat, S.M. Kim, C.R. Müller, Bifunctional core-shell architecture allows stable H<sub>2</sub> production utilizing CH<sub>4</sub> and CO<sub>2</sub> in a catalytic chemical looping process, Appl. Catal. B 258 (2019), 117946, <https://doi.org/10.1016/j.apcatb.2019.117946>.
- [23] S.-K. Otto, K. Kousi, D. Neagu, L. Bekris, J. Janek, I.S. Metcalfe, Exsolved nickel nanoparticles acting as oxygen storage reservoirs and active sites for redox CH<sub>4</sub> conversion, ACS Appl. Energy Mater. 2 (2019) 7288–7298, <https://doi.org/10.1021/acsaem.9b01267>.
- [24] Y. Hu, J. Wu, Y. Han, W. Xu, L. Zhang, X. Xia, C. Huang, Y. Zhu, M. Tian, Y. Su, L. Li, B. Hou, J. Lin, W. Liu, X. Wang, Intensified solar thermochemical CO<sub>2</sub> splitting over iron-based redox materials via perovskite-mediated dealloying-exsolution cycles, Chin. J. Catal. 42 (2021) 2049–2058, [https://doi.org/10.1016/s1872-2067\(21\)63857-3](https://doi.org/10.1016/s1872-2067(21)63857-3).
- [25] K. Kousi, D. Neagu, L. Bekris, E.I. Papaioannou, I.S. Metcalfe, Endogenous nanoparticles strain perovskite host lattice providing oxygen capacity and driving oxygen exchange and CH<sub>4</sub> conversion to syngas, Angew. Chem. Int. Ed. 59 (2020) 2510–2519, <https://doi.org/10.1002/anie.201915140>.
- [26] Ye Zheng, X. Liao, H. Xiao, V. Haribal, X. Shi, Z. Huang, L. Zhu, K. Li, F. Li, H. Wang, X. Chen, Highly efficient reduction of O<sub>2</sub>-containing CO<sub>2</sub> via chemical looping based on perovskite nanocomposites, Nano Energy 78 (2020), 105320, <https://doi.org/10.1016/j.nanoen.2020.105320>.
- [27] D.W. Zeng, Y. Qiu, S. Peng, C. Chen, J.M. Zeng, S. Zhang, R. Xiao, Enhanced hydrogen production performance through controllable redox exsolution within CoFeAlO<sub>x</sub> spinel oxygen carrier materials, J. Mater. Chem. A 6 (2018) 11306–11316, <https://doi.org/10.1039/c8ta02477d>.
- [28] Y.P. Chen, X. Zhu, K.Z. Li, Y.G. Wei, Y.E. Zheng, H. Wang, Chemical looping co-splitting of H<sub>2</sub>O-CO<sub>2</sub> for efficient generation of syngas, ACS Sustain. Chem. Eng. 7 (2019) 15452–15462, <https://doi.org/10.1021/acssuschemeng.9b02996>.
- [29] D. Cui, M. Li, Y. Qiu, L. Ma, D. Zeng, R. Xiao, Improved hydrogen production with 100% fuel conversion through the redox cycle of ZnFeAlO<sub>x</sub> oxygen carrier in chemical looping scheme, Chem. Eng. J. 400 (2020), 125769, <https://doi.org/10.1016/j.cej.2020.125769>.
- [30] Y.F. Sun, S. Dai, High-entropy materials for catalysis: a new frontier, Sci. Adv. 7 (2021) 1600, <https://doi.org/10.1126/sciadv.abg1600>.
- [31] T. Li, Y. Yao, Z. Huang, P. Xie, Z. Liu, M. Yang, J. Gao, K. Zeng, A.H. Brozena, G. Pastel, M. Jiao, Q. Dong, J. Dai, S. Li, H. Zong, M. Chi, J. Luo, Y. Mo, G. Wang, C. Wang, R. Shahbazian-Yassar, L. Hu, Denary oxide nanoparticles as highly stable

- catalysts for methane combustion, *Nat. Catal.* 4 (2021) 62–70, <https://doi.org/10.1038/s41929-020-00554-1>.
- [32] S. Hou, X. Ma, Y. Shu, J. Bao, Q. Zhang, M. Chen, P. Zhang, S. Dai, Self-regeneration of supported transition metals by a high entropy-driven principle, *Nat. Commun.* 12 (2021) 5917, <https://doi.org/10.1038/s41467-021-26160-8>.
- [33] H. Xu, Z. Zhang, J. Liu, C.L. Do-Thanh, H. Chen, S. Xu, Q. Lin, Y. Jiao, J. Wang, Y. Wang, Y. Chen, S. Dai, Entropy-stabilized single-atom Pd catalysts via high-entropy fluorite oxide supports, *Nat. Commun.* 11 (2020) 3908, <https://doi.org/10.1038/s41467-020-17738-9>.
- [34] D. Zhang, H.A. De Santiago, B. Xu, C. Liu, J.A. Trindell, W. Li, J. Park, M. A. Rodriguez, E.N. Coker, J.D. Sugar, A.H. McDaniel, S. Lany, L. Ma, Y. Wang, G. Collins, H. Tian, W. Li, Y. Qi, X. Liu, J. Luo, Compositionally complex perovskite oxides for solar thermochemical water splitting, *Chem. Mater.* 35 (2023) 1901–1915, <https://doi.org/10.1021/acs.chemmater.2c03054>.
- [35] A. Le Gal, M. Vallès, A. Julbe, S. Abanades, Thermochemical properties of high entropy oxides used as redox-active materials in two-step solar fuel production cycles, *Catalysts* 12 (2022), <https://doi.org/10.3390/catal12101116>.
- [36] Y. Gao, M. Zhang, Y. Mao, H. Cao, S. Zhang, W. Wang, C. Sun, Z. Song, J. Sun, X. Zhao, Microwave-triggered low temperature thermal reduction of Zr-modified high entropy oxides with extraordinary thermochemical H<sub>2</sub> production performance, *Energy Convers. Manag.* 252 (2022), <https://doi.org/10.1016/j.enconman.2021.115125>.
- [37] S. Zhai, J. Rojas, N. Ahlborg, K. Lim, M.F. Toney, H.Y. Jin, W.C. Chueh, A. Majumdar, The use of poly-cation oxides to lower the temperature of two-step thermochemical water splitting, *Energy Environ. Sci.* 11 (2018) 2172–2178, <https://doi.org/10.1039/cbee00050f>.
- [38] N. Duan, M. Gao, B. Hua, M. Li, B. Chi, J. Li, J.-L. Luo, Exploring Ni(Mn<sub>1/3</sub>Cr<sub>2/3</sub>)<sub>2</sub>O<sub>4</sub> spinel-based electrodes for solid oxide cells, *J. Mater. Chem. A* 8 (2020) 3988–3998, <https://doi.org/10.1039/c9ta11878k>.
- [39] G. Kresse, J. Furthmüller, Efficiency of ab-initio total energy calculations for metals and semiconductors using a plane-wave basis set, *Comput. Mater. Sci.* 6 (1996) 15–50, [https://doi.org/10.1016/0927-0256\(96\)00008-0](https://doi.org/10.1016/0927-0256(96)00008-0).
- [40] P.E. Blochl, Projector augmented-wave method, *Phys. Rev. B* 50 (1994) 17953–17979, <https://doi.org/10.1103/physrevb.50.17953>.
- [41] J.P. Perdew, K. Burke, M. Ernzerhof, Generalized gradient approximation made simple, *Phys. Rev. Lett.* 77 (1996) 3865–3868, <https://doi.org/10.1103/PhysRevLett.77.3865>.
- [42] G. Kresse, D. Joubert, From ultrasoft pseudopotentials to the projector augmented-wave method, *Phys. Rev. B* 59 (1999) 1758–1775, <https://doi.org/10.1103/PhysRevB.59.1758>.
- [43] H.J. Monkhorst, J.D. Pack, Special points for Brillouin-zone integrations, *Phys. Rev. B* 13 (1976) 5188–5192, <https://doi.org/10.1103/PhysRevB.13.5188>.
- [44] Y. Liu, Y. Ying, L. Fei, Y. Liu, Q. Hu, G. Zhang, S.Y. Pang, W. Lu, C.L. Mak, X. Luo, L. Zhou, M. Wei, H. Huang, Valence engineering via selective atomic substitution on tetrahedral sites in spinel oxide for highly enhanced oxygen evolution catalysis, *J. Am. Chem. Soc.* 141 (2019) 8136–8145, <https://doi.org/10.1021/jacs.8b13701>.
- [45] F. Mirabella, E. Zaki, F. Ivars-Barcelo, X. Li, J. Paier, J. Sauer, S. Shaikhutdinov, H. J. Freund, Cooperative formation of long-range ordering in water Ad-layers on Fe<sub>3</sub>O<sub>4</sub>(111) surfaces, *Angew. Chem. Int. Ed.* 57 (2018) 1409–1413, <https://doi.org/10.1002/anie.201711890>.
- [46] B. Xiao, G. Wu, T. Wang, Z. Wei, Y. Sui, B. Shen, J. Qi, F. Wei, J. Zheng, High-entropy oxides as advanced anode materials for long-life lithium-ion batteries, *Nano Energy* 95 (2022), 106962, <https://doi.org/10.1016/j.nanoen.2022.106962>.
- [47] S. Grimme, J. Antony, S. Ehrlich, H. Krieg, A consistent and accurate ab initio parametrization of density functional dispersion correction (DFT-D) for the 94 elements H–Pu, *J. Chem. Phys.* 132 (2010), 154104, <https://doi.org/10.1063/1.3382344>.
- [48] G. Henkelman, B.P. Uberuaga, H. Jónsson, A climbing image nudged elastic band method for finding saddle points and minimum energy paths, *J. Chem. Phys.* 113 (2011) 9901–9904, <https://doi.org/10.1063/1.3553717>.
- [49] L. Tang, Y. Yang, H. Guo, Y. Wang, M. Wang, Z. Liu, G. Yang, X. Fu, Y. Luo, C. Jiang, Y. Zhao, Z. Shao, Y. Sun, High configuration entropy activated lattice oxygen for O<sub>2</sub> formation on perovskite electrocatalyst, *Adv. Funct. Mater.* 32 (2022) 2112157, <https://doi.org/10.1002/adfm.202112157>.
- [50] O.N. Shebanova, P. Lazor, Raman spectroscopic study of magnetite (FeFe<sub>2</sub>O<sub>4</sub>): a new assignment for the vibrational spectrum, *J. Solid State Chem.* 174 (2003) 424–430, [https://doi.org/10.1016/S0022-4596\(03\)00294-9](https://doi.org/10.1016/S0022-4596(03)00294-9).
- [51] V. D’Ippolito, G.B. Andreozzi, D. Bersani, P.P. Lottici, Raman fingerprint of chromate, aluminate and ferrite spinels, *J. Raman Spectrosc.* 46 (2015) 1255–1264, <https://doi.org/10.1002/jrs.4764>.
- [52] M.A. Laguna-Bercero, M.L. Sanjuan, R.I. Merino, Raman spectroscopic study of cation disorder in poly- and single crystals of the nickel aluminate spinel, *J. Phys. Condens. Matter* 19 (2007), 186217, <https://doi.org/10.1088/0953-8984/19/18/186217>.
- [53] J. Huang, Y. Fu, Y. Zhao, J. Zhang, S. Li, S. Li, G. Li, Z. Chen, Y. Sun, Anti-sintering non-stoichiometric nickel ferrite for highly efficient and thermal-stable thermochemical CO<sub>2</sub> splitting, *Chem. Eng. J.* 404 (2021) 127067, <https://doi.org/10.1016/j.cej.2020.127067>.
- [54] F. Donat, C.R. Müller, CO<sub>2</sub>-free conversion of CH<sub>4</sub> to syngas using chemical looping, *Appl. Catal. B* 278 (2020), <https://doi.org/10.1016/j.apcatb.2020.119328>.
- [55] X. Zhang, C. Pei, X. Chang, S. Chen, R. Liu, Z.J. Zhao, R. Mu, J. Gong, FeO<sub>6</sub> octahedral distortion activates lattice oxygen in perovskite ferrite for methane partial oxidation coupled with CO<sub>2</sub> splitting, *J. Am. Chem. Soc.* 142 (2020) 11540–11549, <https://doi.org/10.1021/jacs.0c04643>.
- [56] X. Xia, W.X. Chang, S.W. Cheng, C.D. Huang, Y. Hu, W.B. Xu, L. Zhang, B. Jiang, Z. H. Sun, Y.Y. Zhu, X.D. Wang, Oxygen activity tuning via FeO<sub>6</sub> octahedral tilting in perovskite ferrites for chemical looping dry reforming of methane, *ACS Catal.* 12 (2022) 7326–7335, <https://doi.org/10.1021/acscatal.2c00920>.
- [57] Y. Long, K. Yang, Z. Gu, S. Lin, D. Li, X. Zhu, H. Wang, K. Li, Hydrogen generation from water splitting over polyfunctional perovskite oxygen carriers by using coke oven gas as reducing agent, *Appl. Catal. B* 301 (2022), 120778, <https://doi.org/10.1016/j.apcatb.2021.120778>.
- [58] T. Zong, L. Li, Y. Han, C. Wang, Y. Kang, M. Tian, C. Huang, X. Wang, Influence of the encapsulation degree of Fe<sup>0</sup> active sites on performance of garnets for chemical looping partial oxidation of CH<sub>4</sub>, *Appl. Catal. B* 312 (2022), 121421, <https://doi.org/10.1016/j.apcatb.2022.121421>.
- [59] B. Yao, T. Xiao, O.A. Makgae, X. Jie, S. Gonzalez-Cortes, S. Guan, A.I. Kirkland, J. R. Dilworth, H.A. Al-Megren, S.M. Alshihri, P.J. Dobson, G.P. Owen, J.M. Thomas, P.P. Edwards, Transforming carbon dioxide into jet fuel using an organic combustion-synthesized Fe-Mn-K catalyst, *Nat. Commun.* 11 (2020) 6395, <https://doi.org/10.1038/s41467-020-20214-z>.
- [60] M. Zhu, T.C.R. Rocha, T. Lunkenbein, A. Knop-Gericke, R. Schlögl, I.E. Wachs, Promotion mechanisms of iron oxide-based high temperature water-gas shift catalysts by chromium and copper, *ACS Catal.* 6 (2016) 4455–4464, <https://doi.org/10.1021/acscatal.6b00698>.
- [61] A.I.M. Rabee, D. Zhao, S. Cisneros, C.R. Kreyenschulte, V. Kondratenko, S. Bartling, C. Kubis, E.V. Kondratenko, A. Brückner, J. Rabeh, Role of interfacial oxygen vacancies in low-loaded Au-based catalysts for the low-temperature reverse water-gas shift reaction, *Appl. Catal. B* 321 (2023), 122083, <https://doi.org/10.1016/j.apcatb.2022.122083>.
- [62] J.S. Elias, K.A. Stoerzinger, W.T. Hong, M. Risch, L. Giordano, A.N. Mansour, Y. Shao-Horn, In situ spectroscopy and mechanistic insights into CO oxidation on transition-metal-substituted ceria nanoparticles, *ACS Catal.* 7 (2017) 6843–6857, <https://doi.org/10.1021/acscatal.7b01600>.
- [63] Y. Zhang, L. Li, Y. Liu, T. Feng, S. Xi, X. Wang, C. Xue, J. Qian, G. Li, A symbiotic hetero-nanocomposite that stabilizes unprecedented CaCl<sub>2</sub>-type TiO<sub>2</sub> for enhanced solar-driven hydrogen evolution reaction, *Chem. Sci.* 10 (2019) 8323–8330, <https://doi.org/10.1039/c9sc01216h>.
- [64] A.R. Kamali, Black diamond powder: on the thermal oxidation and surface graphitization, *Appl. Surf. Sci.* 551 (2021), <https://doi.org/10.1016/j.apsusc.2021.149371>.
- [65] Y. Liu, Y.Y. Zhang, Q.W. Kou, Y. Chen, D.L. Han, D.D. Wang, Z.Y. Lu, L. Chen, J. H. Yang, S. Xing, Eco-friendly seeded Fe<sub>3</sub>O<sub>4</sub>-Ag nanocrystals: a new type of highly efficient and low cost catalyst for methylene blue reduction, *RSC Adv.* 8 (2018) 2209–2218, <https://doi.org/10.1039/c7ra11348j>.
- [66] R.C.C. Costa, F.C.C. Moura, J.D. Ardisson, J.D. Fabris, R.M. Lago, Highly active heterogeneous Fenton-like systems based on Fe<sup>0</sup>/Fe<sub>3</sub>O<sub>4</sub> composites prepared by controlled reduction of iron oxides, *Appl. Catal. B* 83 (2008) 131–139, <https://doi.org/10.1016/j.apcatb.2008.01.039>.
- [67] A. Lak, M. Kraken, F. Ludwig, A. Kornowski, D. Eberbeck, S. Sievers, F.J. Litterst, H. Weller, M. Schilling, Size dependent structural and magnetic properties of FeO-Fe<sub>3</sub>O<sub>4</sub> nanoparticles, *Nanoscale* 5 (2013) 12286–12295, <https://doi.org/10.1039/c3nr04562e>.
- [68] F. Nakagomi, S.W. da Silva, V.K. Garg, A.C. Oliveira, P.C. Morais, A. Franco, Influence of the Mg-content on the cation distribution in cubic Mg<sub>x</sub>Fe<sub>3-x</sub>O<sub>4</sub> nanoparticles, *J. Solid State Chem.* 182 (2009) 2423–2429, <https://doi.org/10.1016/j.jssc.2009.06.036>.
- [69] Q.W.H. Fan, C.D. Huang, S.B. Xi, Y. Yan, J.J. Huang, S. Saqlane, L.G. Tao, Y.H. Dai, A. Borgna, X.D. Wang, W. Liu, Breaking the stoichiometric limit in oxygen-carrying capacity of Fe-based oxygen carriers for chemical looping combustion using the Mg-Fe-O solid solution system, *ACS Sustain. Chem. Eng.* 10 (2022) 7242–7252, <https://doi.org/10.1021/acssuschemeng.2c00271>.
- [70] A.G. Kochur, K.A. Guglev, A.T. Kozakov, S.P. Kubrin, A.V. Nikolskii, V. I. Torgashev, X-ray photoelectron and Mössbauer spectroscopy studies of the valence state of transition metal ions in Co<sub>1-x</sub>Fe<sub>x</sub>Cr<sub>2</sub>O<sub>4</sub> (x = 0.1, 0.2, 0.5) ceramics, *Phys. Solid State* 58 (2016) 108–114, <https://doi.org/10.1134/s1063783416010170>.
- [71] S.N. de Medeiros, A. Luciano, L.F. Cótica, I.A. Santos, A. Paesano, J.B.M. da Cunha, Structural and magnetic characterization of the ball-milled α-Fe<sub>2</sub>O<sub>3</sub>-Mn<sub>2</sub>O<sub>3</sub> and α-Fe-Mn<sub>2</sub>O<sub>3</sub> systems, *J. Magn. Magn. Mater.* 281 (2004) 227–233, <https://doi.org/10.1016/j.jmmm.2004.04.109>.